

# Blade/casing rubbing interactions in aircraft engines: numerical benchmark and design guidelines based on NASA rotor 37

Elsa Piollet<sup>1</sup>, Florence Nyssen<sup>1</sup>, Alain Batailly<sup>1</sup>

## Abstract

In order to improve the efficiency of aircraft engines, the reduction of clearances between blade tips and their surrounding casing is one avenue manufacturers consider to lower aerodynamic losses. This reduction increases the risk of blade tip/casing contact interactions under nominal operating conditions. Designers need tools to accurately predict subsequent nonlinear vibrations. Engineers and researchers have developed a variety of sophisticated numerical models to predict blades' responses. These models are related to distinct frameworks (time/frequency domain) and various solution algorithms (explicit/implicit time integration schemes, penalty/Lagrange multiplier contact treatment...) which calls for comparative analyses. However, published results are often limited for the sake of confidentiality thus preventing any detailed confrontation. While qualitative understanding can be gained from simplified academic models, full scale models are needed to predict complex interactions in a realistic manner. In this context, this paper proposes a benchmark featuring detailed simulations and analyses of a full 3D finite element model based on the open NASA rotor 37 compressor blade to facilitate reproducibility and collaboration across the research community.

NASA rotor 37, a compressor stage widely used as a test case in aerodynamic simulations and validations, has the advantage of presenting a realistic blade geometry. The geometry of the blade is built from publicly available reports. The paper provides details on the geometry, the numerical model and the results to allow an easy use of this model across the fields of structural dynamics.

Two contact scenarios are investigated: one with direct contact against the casing, and one with abradable material deposited on the casing to mitigate contact severity through wear. The nonlinear vibration response of the blade is simulated in the time domain. It is evidenced that the addition of the abradable material decreases the amplitude of vibration for most of the angular speeds investigated. However, new interactions appear for some angular speeds. The obtained results are consistent with previous simulations on industrial geometries.

Based on works showing improved aerodynamic performances when the blade is tilted, a total of seven geometries are investigated: the reference blade, with a straight vertical stacking line similar to the original rotor 37, two forward-leaned blades, two backward-swept blades and two full forward chordwise swept blades. The sweep and lean variations are shown to have a dramatic impact on the vibration response: the backward sweep results in an increased blade's robustness to contact events and the full forward chordwise sweep in a reduced robustness, while the forward lean leads to a robustness similar to the reference blade.

## Keywords

rotor/stator interaction; nonlinear dynamics; compressor blade; sweep; lean

# Interaction de contact aube/carter dans les moteurs d'avion: cas de référence numérique et règles de conception basés sur le rotor 37 de la NASA

Elsa Piollet<sup>1</sup>, Florence Nyssen<sup>1</sup>, Alain Batailly<sup>1</sup>

## Résumé

La réduction des jeux aubes/carter est un des principaux axes de recherche considérés par les ingénieurs pour améliorer le rendement des dernières générations de moteurs d'avion. Un frein évident à cette réduction des jeux est lié au fait qu'elle favorise inévitablement l'apparition de contacts entre les différents composants tournants (tels que les aubes) et fixes (les carters environnants). Plusieurs défis doivent alors être relevés par les concepteurs, notamment la possibilité de prédire numériquement le comportement vibratoire des aubes à la suite de tels contacts. En l'absence d'un cadre théorique unifié pour l'analyse de systèmes mécaniques subissant des contacts structuraux, les différents motoristes ont—dans le cadre de collaborations avec différents centres de recherche—développé des outils numériques en s'appuyant sur des stratégies de résolution variées: paradigmes fréquentiel ou temporel, schémas d'intégration temporelle explicite ou implicite, traitement du contact par multiplicateurs de Lagrange ou méthode de la pénalité... Bien que de nombreux résultats associés à ces différents modèles aient été publiés dans la littérature, les contraintes en termes de confidentialité nuisent fortement à la reproductibilité des analyses effectuées. Dans ce contexte, cet article présente un cas test pour l'analyse de la réponse au contact d'un modèle éléments finis 3D s'appuyant sur une géométrie ouverte: l'aube rotor37 de la NASA. L'objectif est de permettre d'établir un point de comparaison pour différentes méthodes et favoriser ainsi la confrontation des méthodes existantes.

L'aube rotor37 de la NASA, qui a été largement utilisée pour le développement et la validation de méthodes de résolutions de problèmes aérodynamiques, a l'avantage de disposer d'un profil réaliste, représentatif d'une aube de moteur d'avion. Pour cet article, la géométrie de l'aube est construite sur base de rapports publics disponibles en ligne. L'outil utilisé pour la construction du modèle est librement téléchargeable sur le site HAL (<https://hal.archives-ouvertes.fr/hal-02127993>). Deux scénarios de contact sont considérés, avec et sans revêtement abrasable sur le carter (supposé parfaitement rigide). Le comportement vibratoire de l'aube est simulé dans le domaine temporel à l'aide d'un schéma d'intégration temporel explicite. Sur base de travaux relatifs aux performances aérodynamiques de l'aube rotor37, plusieurs variantes du profil sont considérées dans le but de fournir la première étude comparative des performances combinées aérodynamiques et dynamiques en réponse au contact.

## Mots-clés

interaction rotor/stator; dynamique non-linéaire; aube de compresseur; flèche; inclinaison

1 - Département de génie mécanique, École Polytechnique de Montréal, P.O. Box 6079, Succ. Centre-Ville, Montréal, Québec, Canada H3C 3A7

## 1 Introduction

The primary goal of turbomachinery blade design is to increase the turbomachine efficiency in order to reduce fuel consumption. To this end, blade design procedures focus mainly on the aerodynamic performance of blades. Structural considerations are often limited to constraints on stress levels under static loading [1].

Nowadays, the drive towards reduced fuel consumption is motivated both by operating costs and by the need to reduce carbon emissions. One avenue to improve the overall engine efficiency is to reduce aerodynamic losses by minimizing clearances between the rotating blade tips and the surrounding casing [2]. However, reduced tip clearances lead to increased risks of contact between the blades and the casing. Contact events can lead to potentially destructive interactions [3]: single blade vibration (rubbing) [4, 5, 6], full bladed disk and casing vibration with modal interaction [7, 8] or whole engine interactions featuring shaft orbital motion [9, 10, 11, 12].

Solutions to reduce the severity of contact interactions include increasing blade/casing clearances and depositing an abradable coating along the casing contact surface [13, 14, 15]. The first solution contradicts the aerodynamic objectives, as stated above, therefore the use of abradable coating is common in industrial engines. However, it has been observed that blade failure may still occur with abradable coating [4]. Therefore, there is a need for new design criteria in order to manufacture blades that are robust with respect to contact events. Such criteria have to be defined based on reliable prediction methods for contact interactions. As contact interactions are multi-physical, multi-scale and nonlinear, involving vibrations, wear, and thermal effects among others [16], commercial software packages are generally not applicable: as a consequence, ad hoc numerical strategies are developed by most of the engine manufacturers in house or in partnership with academic research laboratories (e.g. Rolls Royce [17, 18, 19], GE Aviation [5, 10, 14] and Safran [12, 20]).

Different numerical strategies can be applied to the prediction of contact interactions: phenomenological approaches [5, 6], analytical models [21, 22], simplified models [6, 23], finite elements through brute force modelling [24] or through a more efficient formulation with reduced order models [20]. Simulations can be carried out in the time domain [17, 23] or in the frequency domain [25, 26]. Contact is managed either with a penalty model [10], with Lagrange multipliers [27] or with the augmented Lagrangian approach [21]. Moreover, some models include the casing dynamics [28] or account for the removal of abradable coating [29]. Are these methods equivalent, and which is more adapted to define design criteria? Comparison is not straightforward: the results from most articles cannot be reproduced because the data is normalized and the geometries are often proprietary. Simplified academic models with no intellectual property restrictions, on the other hand, are generally not representative of realistic rotor geometries. In order to allow a simple comparison between the methods and the obtained results, an open geometry representative of industrial geometries is needed.

The goal of this paper is to propose an open and realistic test case to serve as a benchmark for contact simulations. Such test cases are commonly used in aerodynamics for example, where NASA rotor 37 (a compressor blade) and NASA rotor 67 (a fan blade) are often used to validate numerical methods or to serve as a basis for studies on blade design [30, 31, 32]. The systematic use of a few open geometries not only allows validating numerical methods, it also leads to a sum of works that are directly comparable, that provide a better understanding of the phenomena at stake, and that can be used ultimately to extract design guidelines. Recently, the idea of using open test cases was also introduced in the fields of aerodynamics and flutter in steam turbines [33, 34] and structural dynamics of blades with friction dampers [35]. This latter geometry responds to researchers' needs in nonlinear structural dynamics, but it is not applicable to the case of contact interactions, as a realistic blade geometry is necessary. Indeed, as blade/casing contacts occur along the blade tip, the full blade geometry needs to be realistic to provide relevant responses. In this context, the present paper proposes a numerical benchmark based on a classical aerodynamic test case: NASA rotor 37. As mentioned above, rotor 37 is a known open model used extensively in the aerodynamic literature, and is considered to be a realistic transonic compressor blade geometry [31]. The choice of a compressor blade is consistent with industrial observations of rubbing events occurring mainly at the compressor stage [16].

The proposed benchmark consists in the following elements. (1) The blade is described in details, with all necessary geometry parameters and material properties. The geometry is adaptable to allow exploring the consequences of geometry modifications on contact response. (2) The numerical strategy for contact simulations is presented and all simulation parameters are provided. Detailed simulation results are presented to serve as comparison points. The proposed test case is studied with and without abradable coating over a wide angular frequency range. The results

include the blade tip displacement, the stress field near the root of the blade and abradable wear when applicable. (3) The effect of geometry modification is investigated by comparing seven blades geometries: the reference blade and six blades with sweep and lean variations. These results are used to discuss the consequences of aerodynamic recommendations on contact response, and to outline first guidelines for the design of blades with contact criteria. (4) The seven blade geometries and finite element models, along with the computer program used to generate them, are made publicly available to facilitate reuse and comparisons [36].

The paper is organized as follows. The second section presents the scope of the benchmark, in terms of the numerical method employed and the type of data provided. In the third section, the properties of the blade reference case are described. In the fourth section, the numerical strategy and the corresponding parameters are presented. In the fifth section, contact simulation results are detailed for the reference blade. Finally, in the sixth section, the effect of sweep and lean variations are investigated.

## 2 Scope of the benchmark

This section clarifies the underlying hypotheses and the type of results of the benchmark. Some hypotheses are embedded in the proposed geometries themselves, while other hypotheses are related to the numerical strategy used in this paper.

### 2.1 Geometry

The mechanical system of interest is a compressor blade clamped at its root: the dynamics of the disk and the surrounding blades are neglected. Considering only one blade allows for considerably faster simulations compared to a full bladed disk, and such a model is well suited for the simulation of rubbing events. Indeed, rubbing events typically involve a single structure, be it a blade or a bladed disk [4], and previous works have demonstrated that single blade models led to results in good agreement with experimental measurements [37, 38]. The geometry of the blade itself can be easily modified by varying the parameters describing the profiles at different levels in the blade span, or by modifying the positions of these profiles through sweep and lean variations. In the present article, only the consequences of sweep and lean variations are investigated.

### 2.2 Numerical strategy

The numerical strategy employed to compute the blade response to contact events is detailed in section 4. The key features of this strategy are the following. The computation is made in the time domain in order to capture the transient phenomena involved in the onset of contact interactions. The blade is modelled with a reduced order model computed with the Craig-Bampton method from a finite element model, including centrifugal effects, and contact is managed on retained nodes at the tip of the blade. The casing is considered to be infinitely rigid. Contact is managed with Lagrange multipliers. When accounted for, wear of the abradable coating is described by means of a plastic constitutive law. The capabilities of the employed numerical strategy are summed up in Tab. 1, and the specific capabilities applied in the present article are highlighted.

### 2.3 Results

This paper intends to provide a variety of results against which comparisons can be made. The displacement at the tip of the blade is computed over a wide angular speed range. In the cases with abradable coating, abradable wear at the end of the simulation is analyzed. To allow interpretations closer to industrial needs, the maximal Von Mises stress within the blade is also computed and compared to the blade's yield stress.

## 3 From rotor 37 to the proposed blade model

### 3.1 Rotor 37: a standard test case

#### 3.1.1 General presentation

NASA rotor 37 is a transonic axial flow compressor composed of 36 blades which was initially designed and tested at NASA's Lewis Research Center in the late 1970s [39]: a picture of the experimental rotor is given in Fig. 1.

	rubbing	modal interaction	shaft orbital motion
numerical scheme:			
- time integration	<input checked="" type="checkbox"/>	<input type="checkbox"/>	<input type="checkbox"/>
- frequency approach			
centrifugal effects:			
- stiffness	<input checked="" type="checkbox"/>	<input type="checkbox"/>	<input type="checkbox"/>
- clearance	<input type="checkbox"/>	<input type="checkbox"/>	<input type="checkbox"/>
abradable wear	<input checked="" type="checkbox"/>	<input type="checkbox"/>	<input type="checkbox"/>
gyroscopic effects		<input type="checkbox"/>	<input type="checkbox"/>
variable angular speed	<input type="checkbox"/>	<input type="checkbox"/>	<input type="checkbox"/>
casing dynamics	<input type="checkbox"/>	<input type="checkbox"/>	<input type="checkbox"/>
thermomechanical effects	<input type="checkbox"/>	<input type="checkbox"/>	<input type="checkbox"/>

**Table 1.** capabilities of the employed numerical strategy: available functionalities  and capabilities applied in the present article

The geometry of the blades and experimental aerodynamic measurements performed at NASA were later used to create a blind test case to evaluate the performance of numerical methods in aerodynamics in the 1990s [40]. These experimental measurements now serve as a basis for the validation of numerical methods [30]. As a classical test case representative of complex three-dimensional viscous flow in transonic bladings [31], rotor 37 is also used as an application case for aerodynamic optimization methods [31, 32, 41]. In this sense, rotor 37 constitutes a standard test case in aerodynamics.

Both the representativity and the popularity of NASA rotor 37 make it an ideal blade to define a test case for contact simulations. Original reports provide details on the geometry, and operational conditions that are critical for contact study are also known: the nominal speed is approximated to 1800 rad/s (17188.7 rpm in the original report [39]), and the nominal running clearance is 0.356 mm, which represents 0.45% of the blade span [39]. Moreover, previously published aerodynamic optimizations of rotor 37 will be scrutinized with respect to their responses to contact.

### 3.1.2 Geometry

A meridional view of the rotor is depicted in Fig. 2. The geometry of the blade is defined by stacking 11 profiles from the hub to the blade tip, each profile being described on a surface of revolution with a multiple-circular-arc (MCA) parameterization. The original parameters describing rotor 37 are provided in [43]. Details of this parameterization, including a thorough derivation of corresponding equations, can be found in [44]; the general principle is presented in Fig. 3. Each profile is described on a conical surface of angle  $\alpha$ , in order to be representative of the aerodynamic flow. On the unwrapped conical surface, the centerline of the profile is composed of two segments with a constant turning rate, joined at a transition point where the slope is continuous. Four reference points are used to define the centerline: the inlet, the maximum thickness point, the transition point and the outlet, see Fig. 3. Based on the algorithm proposed by Crouse [44], the following 11 parameters are required for each profile:

- radius and local blade angle for the blade centerline at the inlet/leading edge ( $r_{ic}$  and  $\kappa_{ic}$ ) and at the outlet/trailing edge ( $r_{oc}$  and  $\kappa_{oc}$ );
- local blade angle for the blade centerline at the transition point ( $\kappa_{tc}$ );
- thickness at the inlet, maximum thickness point and outlet ( $t_i$ ,  $t_m$  and  $t_o$ );
- axial position of the maximum thickness point, transition point and outlet with respect to the inlet ( $z_{mc}-z_{ic}$ ,  $z_{tc}-z_{ic}$  and  $z_{oc}-z_{ic}$ ).

The cone angle  $\alpha$  and turning rates  $C_1$  and  $C_2$  are obtained from the aforementioned parameters. The three-dimensional blade is obtained by stacking the profiles so that their centers of gravity are vertically aligned along a straight line with no lean or sweep, see Fig. 2.

## 3.2 Proposed blade model



Figure 1. picture of NASA rotor 37 [42]

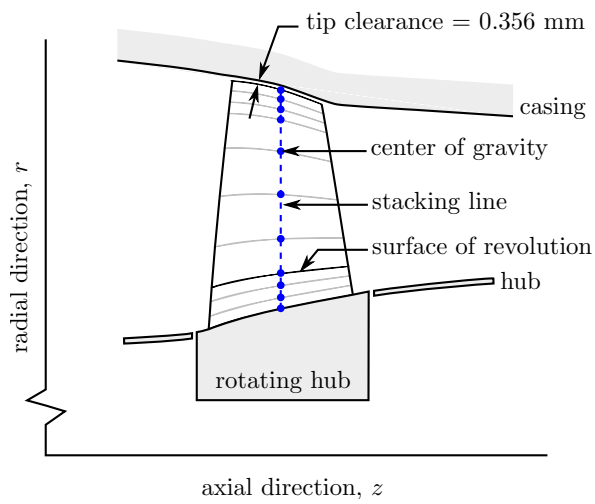


Figure 2. meridional view of NASA rotor 37, adapted from [45]

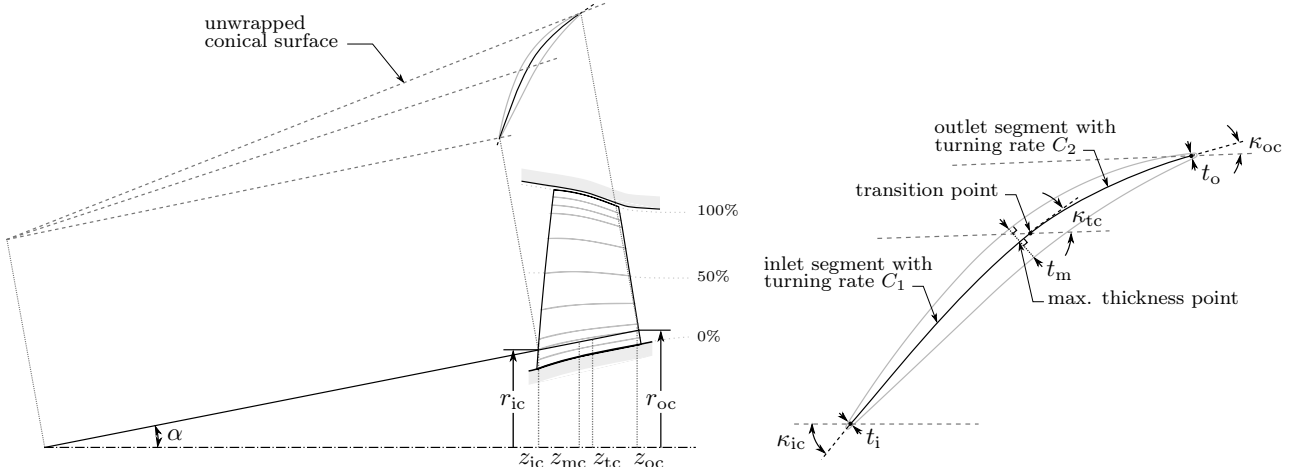


Figure 3. multiple-circular-arc parameterization principle, adapted from [39]

### 3.2.1 Blade geometry

Building rotor 37 geometry from the MCA parameters reported in [43] requires using the algorithm described in a report by Crouse [44], which also provides a printed Fortran IV program implementing the algorithm. For the present work, this program was re-implemented in Python in order to explore easily the consequences of any parameter modification on nonlinear vibration simulations; this program, along with the generated geometries, is publicly available [36].

In order to obtain a smoother geometry, the parameters provided in [43] are modified as follows: for each of the four reference points (inlet, maximum thickness point, transition point and outlet), parameters  $z$ ,  $t$  and  $\kappa$  are smoothed with respect to the corresponding parameter  $r$  with a cubic polynomial. The smoothed parameters are given in Tab. 2<sup>1</sup>. The reference blade studied in the following is obtained from these parameters, and the abbreviated name “Ref” is used to identify it.

<sup>1</sup>Note that the order of parameters is reversed compared to the original report [43], for consistency with the algorithm from [44] in which the hub serves as the reference profile for the stacking procedure: 0% is the hub and 100% is the tip of the blade

% span	$r_{ic}$ (cm)	$r_{oc}$ (cm)	$\kappa_{ic}$ (deg)	$\kappa_{tc}$ (deg)	$\kappa_{oc}$ (deg)	$t_i$ (cm)	$t_m$ (cm)	$t_o$ (cm)	$z_{mc}-z_{ic}$ (cm)	$z_{tc}-z_{ic}$ (cm)	$z_{oc}-z_{ic}$ (cm)
100	25.230	24.502	62.246	62.480	50.008	0.025	0.175	0.025	1.719	1.725	2.672
95	24.935	24.218	61.651	61.861	49.100	0.026	0.186	0.026	1.721	1.705	2.759
90	24.597	23.932	60.988	61.162	48.180	0.027	0.199	0.028	1.726	1.687	2.846
85	24.254	23.644	60.334	60.421	47.242	0.029	0.211	0.029	1.734	1.672	2.933
70	23.211	22.774	58.470	57.953	44.176	0.032	0.250	0.033	1.769	1.643	3.187
50	21.761	21.622	56.190	54.212	39.090	0.037	0.303	0.038	1.834	1.631	3.517
30	20.246	20.468	54.204	50.406	32.168	0.042	0.360	0.043	1.899	1.627	3.836
15	19.030	19.602	52.910	47.831	25.329	0.047	0.407	0.047	1.932	1.608	4.068
10	18.603	19.313	52.520	47.061	22.666	0.048	0.424	0.049	1.936	1.594	4.143
5	18.161	19.026	52.152	46.367	19.805	0.050	0.442	0.050	1.936	1.575	4.218
0	17.780	18.740	51.864	45.837	16.726	0.051	0.459	0.051	1.932	1.553	4.292

Table 2. multiple-circular-arc parameters for the 11 profiles of the reference blade

### 3.2.2 Material properties

Rotor 37 is made of 200-grade maraging steel [39], a nickel alloy. A 18Ni 200-maraging is therefore selected for the proposed blade, and the following average properties are obtained from various reports [46, 47, 48, 49]: modulus of elasticity  $E = 180$  GPa, density  $\rho = 8000$  kg/m<sup>3</sup> and Poisson's ratio  $\nu = 0.3$ . By definition, the 200-grade maraging steel has a yield stress  $\sigma_Y = 200,000$  psi, corresponding to  $\sigma_Y = 1.38$  GPa.

### 3.2.3 Blade dynamics

The first natural frequencies of the proposed blade, computed with centrifugal effects, are plotted on a Campbell diagram in Fig. 4. The first three modes are identified as being the first bending mode (1B), first torsion mode (1T) and second bending mode (2B) from the corresponding modal deformations presented in Fig. 5. For these three first modes, the differences in natural frequencies between the proposed blade and the original rotor 37 [39] are 8.3%, 1.4% and 9.0% respectively. Indeed, it is important to bear in mind that while the proposed blade is based on rotor 37 and presents a similar behaviour, it is not exactly rotor 37. The differences between the original rotor 37's and the proposed blade's frequencies can be explained by the geometry smoothing performed, by uncertainties on the material properties and by the simplification of the boundary conditions at the blade hub for the numerical model. These differences in modal frequencies lead to differences in the angular speeds of interactions between the modes and engine order excitation. In particular, the interaction between the first bending mode and the fourth engine order excitation, which is the focus of the following study, occurs at 1672 rad/s for the proposed blade while it occurs at 1518 rad/s for the original rotor 37 [39].

## 4 Numerical strategy

### 4.1 Overview

The equation of motion to be solved for the blade is the following:

$$\mathbf{M}\ddot{\mathbf{u}} + \mathbf{D}\dot{\mathbf{u}} + \mathbf{K}(\Omega)\mathbf{u} + \boldsymbol{\lambda}_c = \mathbf{F}_e \quad (1)$$

where  $\mathbf{M}$ ,  $\mathbf{D}$  and  $\mathbf{K}(\Omega)$  are respectively the mass, damping and stiffness matrices of the blade,  $\Omega$  is the angular velocity,  $\mathbf{u}$  is the displacement vector,  $\boldsymbol{\lambda}_c$  stands for the contact forces and  $\mathbf{F}_e$  stands for the external forces.

At each time step, the numerical strategy consists in solving Eq. (1) in the time domain to obtain a first prediction of the displacements, and correcting the predicted displacements by applying the necessary contact forces to ensure that no penetration occurs between the blade and the casing or the abradable coating. In the present case, no aerodynamic forcing is considered, therefore  $\mathbf{F}_e = 0$ : the blade vibrates only under the effect of repeated contacts with the casing. The following sections detail the obtention of  $\mathbf{M}$ ,  $\mathbf{D}$  and  $\mathbf{K}(\Omega)$  from the blade geometry, the contact scenarios, the time integration scheme used to solve this equation and the parameters of the simulation. This numerical strategy is the same as detailed in previous publications [37].

### 4.2 Blade modelling

#### 4.2.1 Finite element model

The 3D geometry of the blade and a corresponding finite element mesh are generated in Salome, an open source CAD and meshing software [50]. The blade is described with a finite element model composed of quadratic pentahedra only. The mesh of the reference blade contains 20,657 nodes, and is presented in Fig. 6. Convergence of simulations with respect to the mesh was carefully checked.

#### 4.2.2 Reduced-order model

For numerical efficiency, a reduced-order model (ROM) is computed from the finite element model. The Craig-Bampton method is used, which allows keeping physical nodes along the blade tip for contact management. Eight boundary nodes are selected along the blade tip, regularly spaced from the leading edge to the trailing edge as shown in Fig. 6.

Centrifugal effects are taken into account both in the definition of the Craig-Bampton reduction basis and in the computation of the stiffness matrix which is computed at three angular speeds  $\Omega = 0$ ,  $\Omega = \Omega_{\max}/2$  and

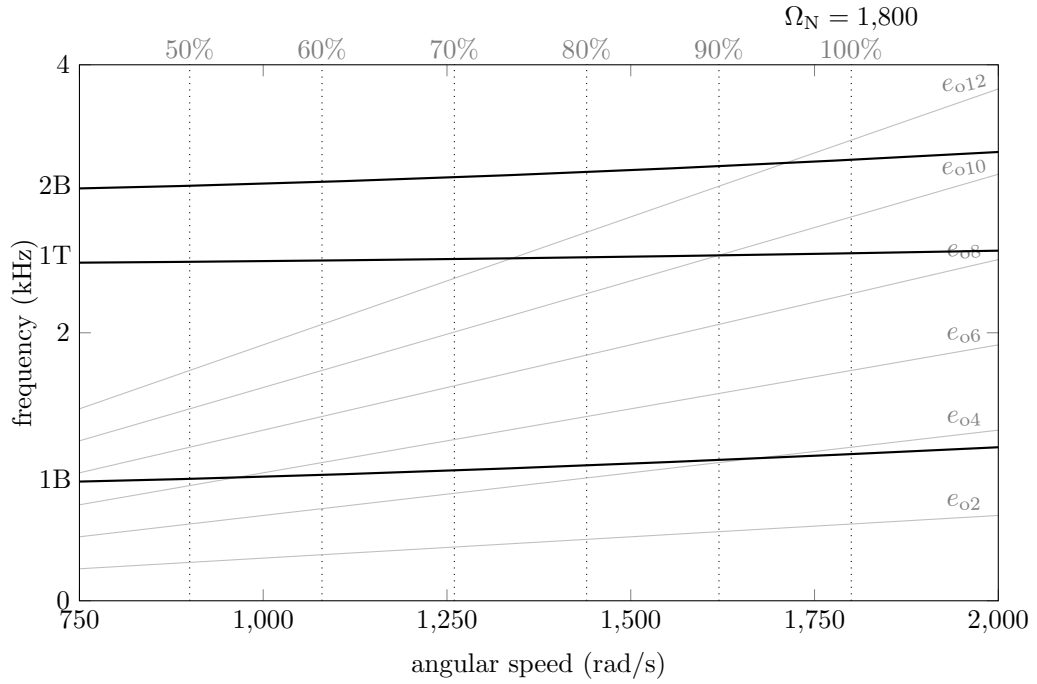


Figure 4. Campbell diagram of the reference blade

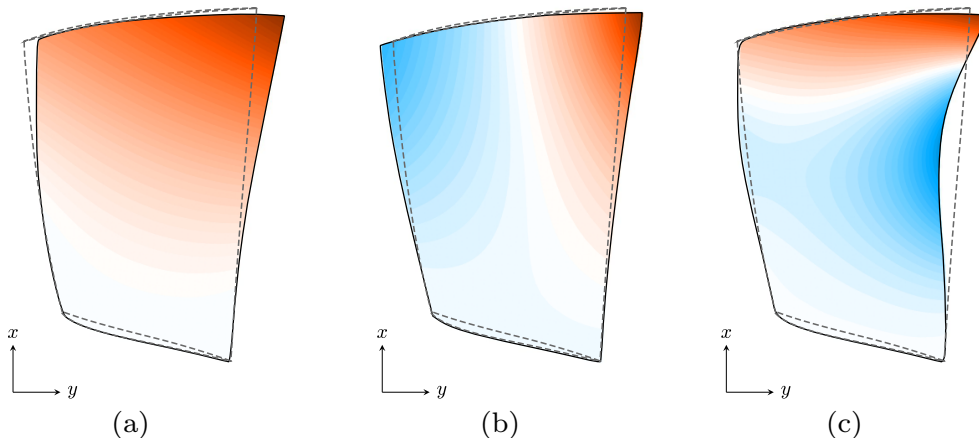


Figure 5. first three normal modes of the reference blade: (a) first bending mode (1B), (b) first torsion mode (1T) and (c) second bending mode (2B)

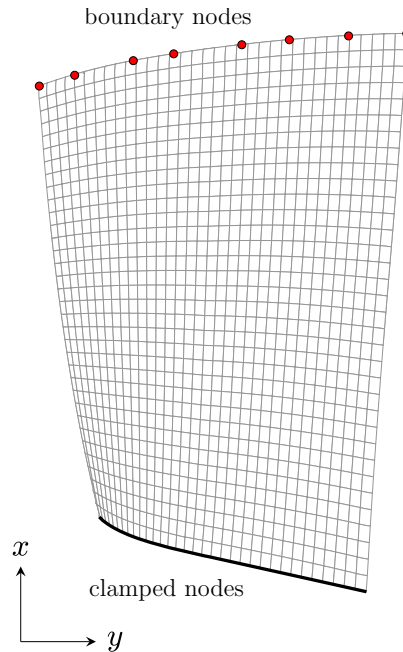


Figure 6. finite element mesh of the reference blade

$\Omega = \Omega_{\max}$  [38]. From the mass and stiffness matrices, fixed-interface and constraint modes are computed for each angular speed. A Gram-Schmidt orthonormalization procedure is then applied to ensure a proper conditioning of the resulting ROM. In the present case, the ROM is already well-conditioned and this orthonormalization procedure does not result in a reduction of the model dimensions. The resulting number of degrees of freedom in the reduced model is  $3 \times 3 \times n_b + 3 \times \eta$ , with  $n_b$  the number of boundary nodes and  $\eta$  the number of retained modes for each angular speed. The stiffness matrix at angular speed  $\Omega$  is expressed as a second degree polynomial in  $\Omega^2$ , based on [51]:

$$\mathbf{K}(\Omega) = \mathbf{K}_0 + \mathbf{K}_1\Omega^2 + \mathbf{K}_2\Omega^4 \quad (2)$$

where the matrices  $\mathbf{K}_0$ ,  $\mathbf{K}_1$  and  $\mathbf{K}_2$  are obtained from linear combination of matrices obtained at  $\Omega = 0$ ,  $\Omega = \Omega_{\max}/2$  and  $\Omega = \Omega_{\max}$ . This interpolation is exact under the hypotheses of a linear computation of centrifugal effects and a constant angular speed  $\Omega$ .

The damping matrix  $\mathbf{D}$  is computed in the modal domain with a single damping coefficient  $\xi$ : in the modal domain,  $\mathbf{D}$  is diagonal with terms  $2\xi\omega_i$  where  $\omega_i$  is the undamped natural frequency of the  $i^{\text{th}}$  mode. This empirical damping formulation is consistent with industrial practice.

### 4.3 Contact scenarios

#### 4.3.1 Contact management

Two contact scenarios are considered:

- blade/casing contact with abradable coating: as is often the case in the industry, an abradable coating is deposited on the casing to reduce impact severity; abradable wear is managed through the use of massless compression elements with a plastic law, as described in [52]; in the case when the abradable is locally fully worn off, the scenario of direct blade/casing contact is considered;
- direct blade/casing contact: this corresponds to the case where no abradable coating is used; in this case, the blade impacts the casing directly.

### 4.3.2 Contact initiation

At the beginning of the simulation, the casing is perfectly circular. Then, a distortion is progressively applied to the casing in order to initiate contact between the blade and the casing, while ensuring that no penetration exists at the beginning of the simulation. This distortion corresponds to an ovalization of the casing, with two zones around angular positions  $\theta = \pi/2$  and  $\theta = 3\pi/2$  respectively where the clearances become negative, as illustrated in Fig. 7. At angular position  $\theta$ , the shape of the distortion is defined as:

$$f(\theta) = \exp \left[ - \left( \frac{(\theta \bmod \pi) / \pi - 0.5}{0.15} \right)^2 \right] \quad (3)$$

For an operating clearance  $c_0$ , if the maximal penetration is equal to the clearance, the gap between the blade and the casing,  $g_c$ , and the gap between the blade and the abradable coating,  $g_a$ , can be expressed as:

$$g_c(\theta, t) = c_0 - 2c_0(1 - e^{-\alpha t})f(\theta) + e_0 - u_r(t) \quad (4)$$

$$g_a(\theta, t) = c_0 - 2c_0(1 - e^{-\alpha t})f(\theta) + (e_0 - e(\theta, t)) - u_r(t) \quad (5)$$

where  $u_r(t)$  is the radial displacement of the considered node,  $e_0$  is the initial thickness of the abradable coating,  $e(\theta, t)$  is the current thickness of the abradable coating after wear, and  $\alpha > 0$  is a coefficient chosen so that the ovalization reaches 0.99 of maximal distortion at 20% of the total simulation time [38].

### 4.4 Contact algorithm

The numerical strategy relies on the explicit central difference time integration scheme and contact is managed through the use of Lagrange multipliers [27]. At each time step  $n + 1$ , the displacements are first linearly predicted from the dynamic equation of the blade Eq. (1) as follows:

$$\mathbf{u}_{n+1}^* = \mathbf{A}\mathbf{u}_n + \mathbf{B}\mathbf{u}_{n-1} \quad (6)$$

with:

$$\mathbf{A} = \left[ \frac{\mathbf{M}}{h^2} + \frac{\mathbf{D}}{2h} \right]^{-1} \left[ \frac{2\mathbf{M}}{h^2} - \mathbf{K} \right] \quad (7)$$

$$\mathbf{B} = \left[ \frac{\mathbf{M}}{h^2} + \frac{\mathbf{D}}{2h} \right]^{-1} \left[ \frac{2\mathbf{M}}{h^2} - \frac{\mathbf{M}}{h^2} \right] \quad (8)$$

where  $h$  is the time step.

The predicted displacements are then used to evaluate the gap between the blade and the abradable coating, and between the blade and the casing, see Eq. (4) and (5). If penetrations are detected between the boundary nodes and the abradable coating, contact forces  $\boldsymbol{\lambda}_{n+1}$  are computed through the use of massless compression elements with a plastic law, as described in [52], which also includes a local modification of the abradable coating thickness to account for abradable removal. If penetrations are detected between the boundary nodes and the casing, contact forces  $\boldsymbol{\lambda}_{n+1}$  are computed through the use of Lagrange multipliers, and details can be found in [27, 53]. In both cases, in the tangential and axial directions, contact forces are computed with the Coulomb law, under the hypothesis of sliding friction; this hypothesis is consistent with the fact that the tangential speed due to rotation is significantly larger than the vibration amplitudes.

The contact forces  $\boldsymbol{\lambda}_{n+1}$  are then used to correct the non-admissible displacements:

$$\mathbf{u}_{n+1} = \mathbf{u}_{n+1}^* + \mathbf{C}\boldsymbol{\lambda}_{n+1} \quad (9)$$

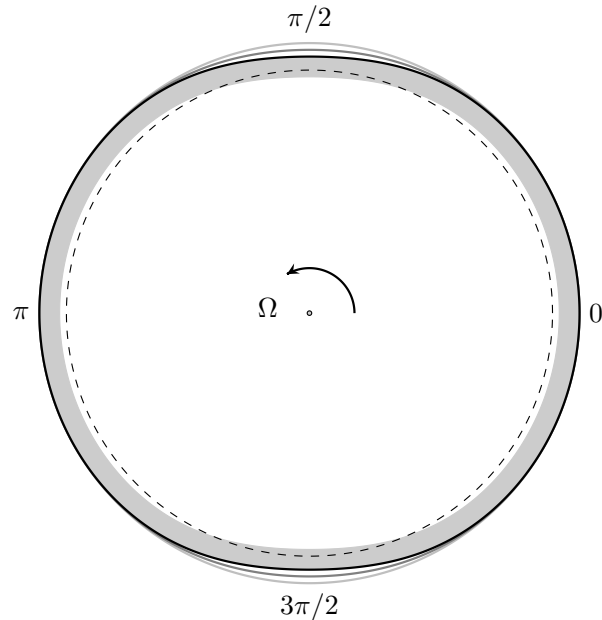


**Figure 7.** casing ovalization (not to scale): at the beginning of the simulation, the casing is perfectly circular (—), then a distortion is progressively applied (—, —) which leads to zones with negative clearances between the blade trajectory (⋯) and the abrasible coating (■)

where  $\mathbf{C}$  is defined as:

$$\mathbf{C} = \left[ \frac{\mathbf{M}}{h^2} + \frac{\mathbf{D}}{2h} \right]^{-1} \quad (10)$$

By definition of the contact forces, this correction leads to admissible displacements with no penetration between the blade and the casing or the abrasible coating.

#### 4.5 Parameters of the simulations

A wide angular speed range is investigated, by performing simulations with a constant angular speed ranging from 750 rad/s to 2000 rad/s with a step of 1 rad/s. For each angular speed, 200 revolutions are simulated with a time step of  $h = 10^{-7}$  s. The rotor modal damping is  $\xi = 0.0005$ . The reduction parameter for the Craig-Bampton method is  $\eta = 10$ , with  $n_b = 8$  boundary nodes, which leads to matrices with dimensions  $102 \times 102$ .

The abrasible coating thickness is 5 mm with 10,000 abrasible elements along the casing circumference. The clearance is set to 0.356 mm, as for the original rotor 37: in the case with abrasible coating, this corresponds to the distance between the blade tip and the abrasible coating, while in the case without abrasible coating this corresponds to the distance between the blade tip and the casing. The penetration due to casing ovalization is equal to the clearance, as illustrated in Fig. 7.

The contact parameters are equal to those used in [37], in which the numerical strategy was compared with experimental results. For both direct contact and contact with the abrasible coating, friction is modelled using a Coulomb law, with a friction coefficient  $\mu = 0.15$ . Mechanical parameters of the abrasible plastic law are the following:

- Young's modulus is  $E = 20$  GPa;
- plastic modulus is  $K = 5$  GPa;
- yield stress is  $\sigma_Y = 1.5$  Pa.

The numerical convergence of the simulations with respect to the time step and the reduction parameters has been checked carefully but is not detailed here for brevity. Detailed demonstration of the convergence of the method can be found in [52].

## 5 Reference blade analysis

### 5.1 Blade tip radial displacement

The first quantity of interest when analyzing the contact simulations is the blade tip radial displacement. Indeed, blade tip radial displacement is associated with the blade tip getting closer and further from the casing, and large radial displacements may indicate repeated contacts between the blade and the casing, and may be related to high stress levels in the blade (see section 5.2). For each angular speed, the simulated radial displacement is analyzed in two steps: first, the overall displacement level is computed to obtain an indication of the criticality of the specific angular speed; secondly, the frequency content of the displacement signal is analyzed in order to identify the phenomena at stake. The root-mean-square (rms) level of the radial displacement at the leading edge of the blade tip over the last 100 revolutions is plotted in Fig. 8b as a function of the angular speed for the case with direct contact and the case with abrasable coating. The Fourier transform is then used to obtain the frequency content of the displacement signals, and spectral maps are created by plotting the resulting spectra as a function of the angular speed in Fig. 8a (direct contact) and 8c (contact with abrasable coating). Both maps have the same color map, with white corresponding to lower amplitudes  $a_{\min}$  and black to higher amplitudes  $a_{\max}$ .

For the case with direct contact, the rms level increases with the angular speed up to 1344 rad/s (Fig. 8b), then decreases suddenly at 1345 rad/s and remains low for higher angular speeds. This large modification of the response level for a small change of one operational parameter, sometimes called a jump, is characteristic of nonlinear mechanical systems. The spectral map, Fig. 8a, shows lines of higher amplitudes corresponding mainly to even harmonics of the angular speed (even engine orders in Fig. 4), which is consistent with the fact that the ovalization leads to an excitation occurring twice per revolution. Contributions of odd harmonics of the angular speed are also visible around 1500 rad/s for example, and non-integer harmonics of the angular speed are also visible around 1900 rad/s, which can be related to the nonlinear nature of the phenomena at stake. The intersection of the modes of the blade with engine orders do not lead explicitly to higher amplitudes of vibration.

For the case with abrasable coating, the rms level (Fig. 8b) shows 4 peaks of higher amplitudes with maxima at 838 rad/s, 996 rad/s, 1264 rad/s and 1717 rad/s, which correspond to intersections between the first bending and engine orders 7, 6, 5 and 4 respectively (noted  $1B/e_{o7}$ ,  $1B/e_{o6}$ ,  $1B/e_{o5}$  and  $1B/e_{o4}$ ), as visible on the spectral map Fig. 8c. The corresponding angular speeds are compared with the angular speeds predicted from the Campbell diagram in Tab. 3. As can be observed, the simulated interaction speeds are higher than those predicted from the Campbell diagram, which is a consequence of the contact stiffening phenomenon. The rms level (Fig. 8b) and spectral map (Fig. 8c) also indicate interactions with the first torsion mode, at 1630 rad/s for example, though they lead to lower radial displacement at the tip of the blade. Jumps are visible with large amplitude variations between two angular speeds, especially after the interactions. For angular speeds outside of the identified interactions, the rms level is significantly lower for the case with abrasable coating than for the case with direct contact.

This analysis shows that the addition of an abrasable coating on the casing leads to lower amplitudes of vibration for most angular speeds, but also leads to higher vibration amplitudes on narrow ranges of angular speeds. Therefore, the abrasable coating plays its role of mitigating the consequences of contact events at most angular frequencies,

	Campbell	max. rms
$\Omega_{1B/e_{o7}}^{\text{Ref}}$ (rad/s)	806	838
$\Omega_{1B/e_{o6}}^{\text{Ref}}$ (rad/s)	965	996
$\Omega_{1B/e_{o5}}^{\text{Ref}}$ (rad/s)	1213	1264
$\Omega_{1B/e_{o4}}^{\text{Ref}}$ (rad/s)	1672	1717

**Table 3.** interaction speeds corresponding to the  $1B/e_{o7}$ ,  $1B/e_{o6}$ ,  $1B/e_{o5}$  and  $1B/e_{o4}$  intersections, obtained from the Campbell diagrams and from the speed at maximal radial displacement

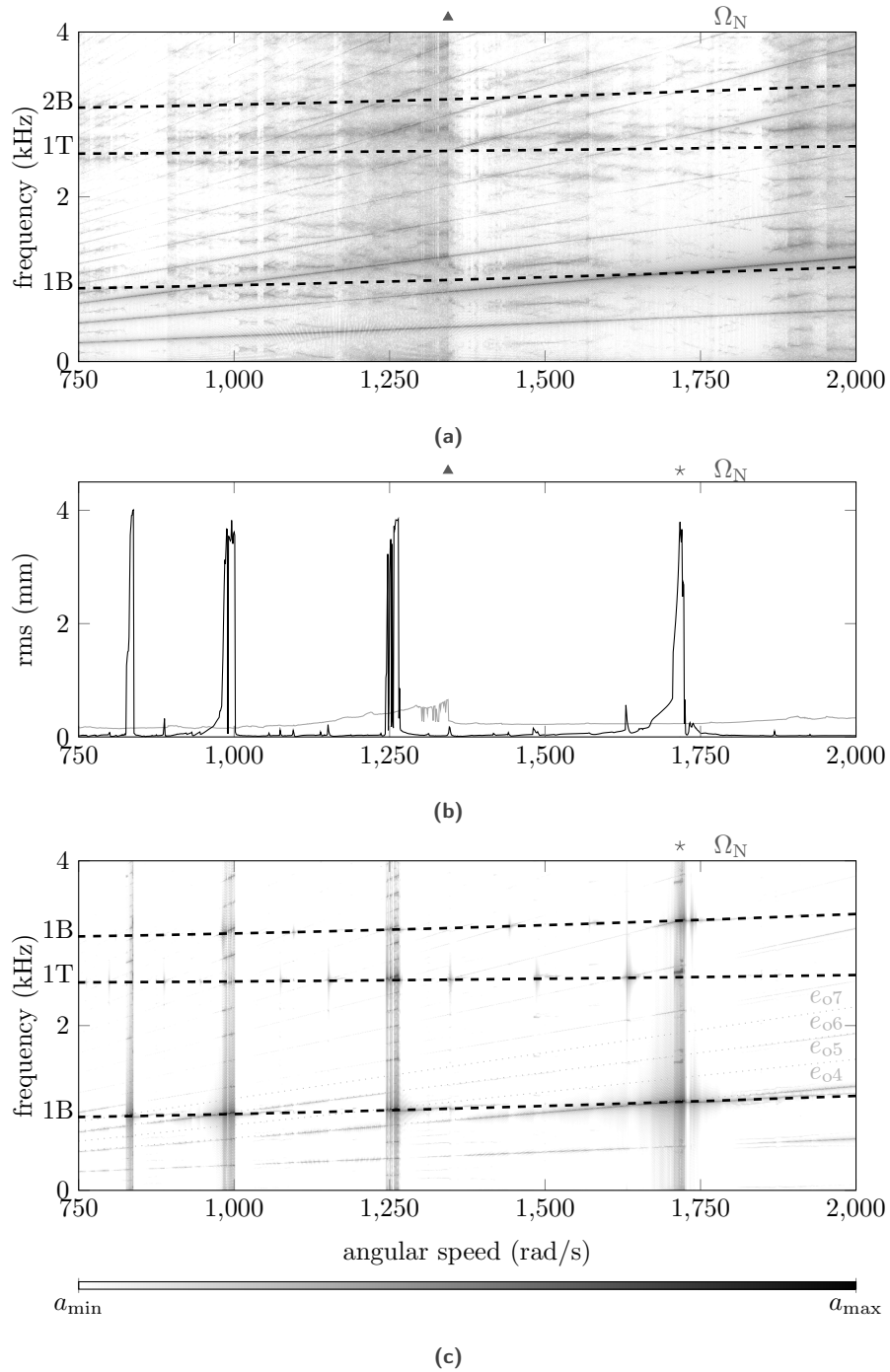


**Figure 8.** radial displacement at the leading edge: (a) spectral map for the case with direct contact, (b) rms levels and (c) spectral map for the case with abrasible coating

but these results suggest that detrimental interactions may occur around specific angular speeds, which is consistent with experimental observations [37]. Previous studies have related these interactions with the removal of abradable coating which modifies the contact configuration and may lead to successive synchronizations and desynchronizations of the contacts with the blade modes [38].

Based on this first analysis, specific angular speeds are selected for subsequent investigations, and are highlighted in Fig. 8. For the case with direct contact, the speed of highest rms level,  $\Omega_{\text{direct}}^{\text{Ref}} = 1344$  rad/s ( $\blacktriangle$ ), is selected. For the case with abradable coating, the speed of interaction 1B/ $e_{o4}$ ,  $\Omega_{1B/e_{o4}}^{\text{Ref}} = 1717$  rad/s ( $\star$ ), is selected, as it is one of the four high-amplitude interactions identified. Finally, the speed  $\Omega_N = 1800$  rad/s is also selected as it correspond to the nominal speed of the original rotor 37.

## 5.2 Von Mises stress

From an industrial perspective, the maximal stress level in a blade is a critical information. Indeed, if the maximal stress level exceeds the yield stress of the blade material, irreversible deformations will occur, which may lead eventually to blade failure. The employed numerical strategy allows transforming the simulations on the reduced order model back into the finite element domain to compute stresses within the blade at each time step.

### 5.2.1 Stress computation

Stress post-processing is performed on a submesh of the blade at downsampled time steps for efficiency. In order to define the appropriate submesh and downsampling, analyses are first performed on the whole blade. As an example, post-processing is shown in Fig. 9 for the 100<sup>th</sup> revolution of the simulation with abradable coating at angular speed 1717 rad/s, with 248 points over the revolution. Then, downsampling is applied and the 62 post-processed points are represented on the same figure. Finally, the stress level is computed again on the submesh presented in Fig. 10, and results are represented in Fig. 9. Post-processing over 62 points corresponds to sampling frequencies of 7485 Hz to 20161 Hz for angular speeds ranging from 750 rad/s to 2000 rad/s respectively. This comparison shows that the selected submesh leads to identical maximal stress  $\sigma_{\text{max}}$ , and that reasonable downsampling has a limited effect on the identified maximal stress over the revolution (a difference of 1.1% is found for the value of  $\sigma_{\text{max}}$ ).

The submesh contains 1414 nodes and 415 elements and is defined as follows:

- *nodes*: all nodes such as  $x < 19.7$  cm,  $1.65$  cm  $< z < 2.65$  cm (with  $x = 0$  at the rotor axis and  $z = 0$  at the hub profile leading edge), excluding clamped nodes at the root of the blade;
- *elements*: elements whose all constitutive nodes are included in the above selection.

In the following, only the maximal Von Mises stress over the submesh is retained for each post-processed time step. Results are normalized with respect to the yield stress  $\sigma_Y = 1.38$  GPa.

For each angular speed, stresses are computed over the last revolution as an indication of the overall level during the simulation: if the yield stress is reached on the last revolution, then it is reached at least at one point of the simulation, and while the opposite is not necessarily true, it can be assumed that if stress is significantly under the yield stress on the last revolution then the yield stress may only have been encountered during the transient phase and for a limited number of revolutions. For the selected angular speeds, stresses are computed over the first revolutions in order to identify whether and when the yield stress is exceeded. The provided stress on a given revolution corresponds to the maximal stress over the 62 post-processed points.

### 5.2.2 Transient evolution of stress at specific angular speeds

The evolution of the maximum Von Mises stress within the blade is plotted in Fig. 11 over the first 100 revolutions, and the last revolution, at 1344 rad/s for the case with direct contact and at 1717 rad/s for the case with abradable coating. As for all simulations, due to the progressive ovalization of the casing, contact only occurs after a certain time corresponding to about 7 blade revolutions. Once contact is initiated, both cases exhibit generally increasing stress levels. At the beginning, the case with direct contact exhibits higher stress levels, but after the 19<sup>th</sup> revolution the stress is higher for the case with abradable coating. Overall, the case with direct contact leads to lower levels of stress. The case with abradable coating leads to a stress level exceeding the yield stress after 40 revolutions, while the yield stress is reached slightly before the 90<sup>th</sup> revolution in the case without abradable coating. As anticipated from the analysis of radial displacements, the case with abradable coating is more detrimental when considering interactions.

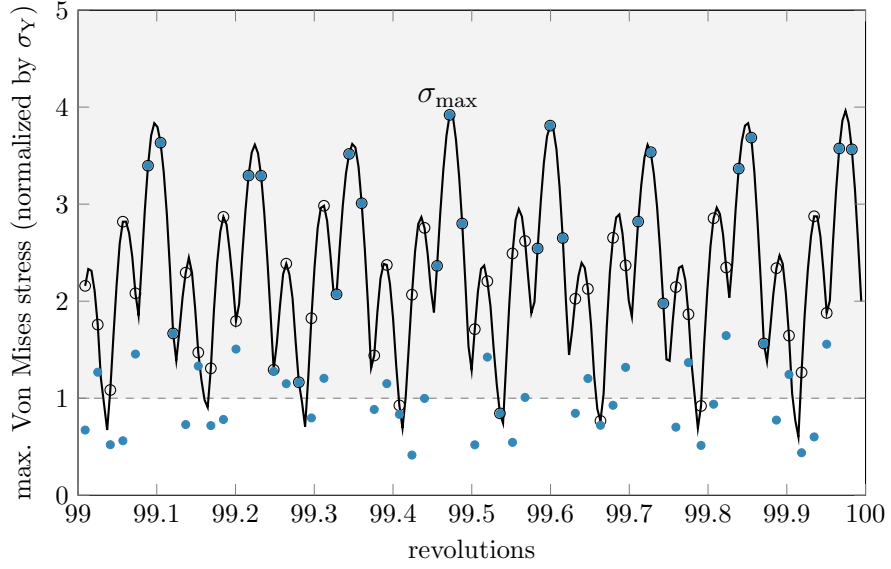


**Figure 9.** maximal Von Mises stress  $\sigma_{\max}$  during the 100<sup>th</sup> revolution for the case with abradable coating: maximal stress within the whole blade computed at 248 time steps (—) and 62 time steps (○), and computed within the submesh at 62 time steps (●);  $\sigma_Y = 1.38$  GPa

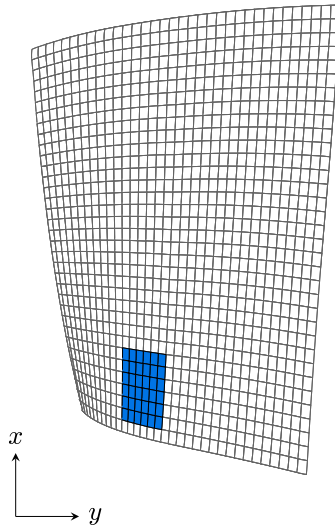


**Figure 10.** submesh on which Von Mises stresses are computed, in blue

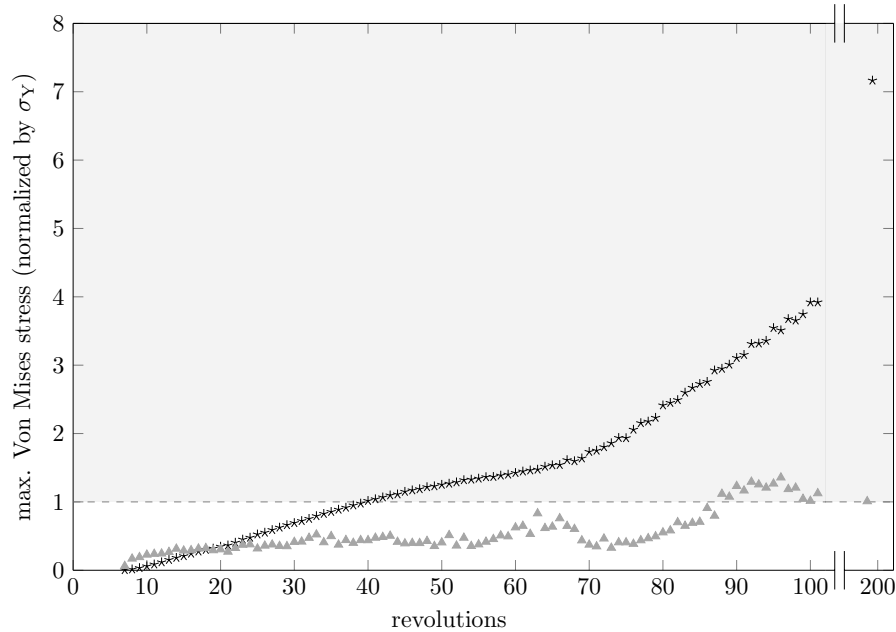


**Figure 11.** maximal Von Mises stresses for the case with direct contact at  $\Omega_{\text{direct}}^{\text{Ref}} = 1344$  rad/s ( $\blacktriangle$ ) and for the case with abrasion coating at  $\Omega_{1B/e_{o4}}^{\text{Ref}} = 1717$  rad/s ( $\star$ );  $\sigma_Y = 1.38$  GPa

At nominal speed  $\Omega_N = 1800$  rad/s, the stress levels for both cases remain below the yield stress for the whole simulation, as shown in Fig. 12. This is an important result, as it indicates that outside of interactions, contact does not lead to immediate risks of blade failure. Moreover, this confirms the applicability of simulations carried out with linear finite element models for these angular speeds. Comparing both cases, stress level is significantly decreased by the addition of the abrasion coating. In the case with direct contact, stress levels are higher, especially at the beginning of the interaction.

### 5.2.3 Wide angular speed range

The maximal stresses over the last revolution for each angular speed from 750 rad/s to 2000 rad/s are plotted in Fig. 13 for both cases with direct contact and with abrasion coating. In both cases, most simulations end with stress levels under the yield stress. Around interaction speeds identified from radial displacement, stress levels are higher than the yield stress, which confirms that such interactions may be detrimental to the blade integrity. Outside of interaction angular speed ranges, simulations with abrasion coating lead to significantly lower levels of stress in the blade, as was already observed for nominal speed in Fig. 12. While stress levels are under the yield stress in both cases, in the case with direct contact the combination of higher stress levels and frequency content at higher frequencies (Fig. 8a) may lead to high cycle fatigue (HCF) of the blade. Therefore, the configuration with abrasion coating is beneficial, as long as the blade is designed so that interactions are not encountered during the blade operation. In practice, interaction crossings may occur: specific simulations with variable angular speed would be necessary to identify their consequences, but are beyond the scope of the present paper.

### 5.3 Abradable wear

By definition, the role of the abrasion coating is to act as a sacrificial material which wears off when impacted by the blade, in order to mitigate contact severity. The final level of wear of the abrasion coating can be measured at the end of experimental tests [37, 38], and it provides information on the type of interaction that occurred as deeper lobes are created at positions where the blade have impacted repeatedly. During the interaction, the direct consequence of abrasion wear is a modification in blade/abrasion clearances. From a structural dynamics point of

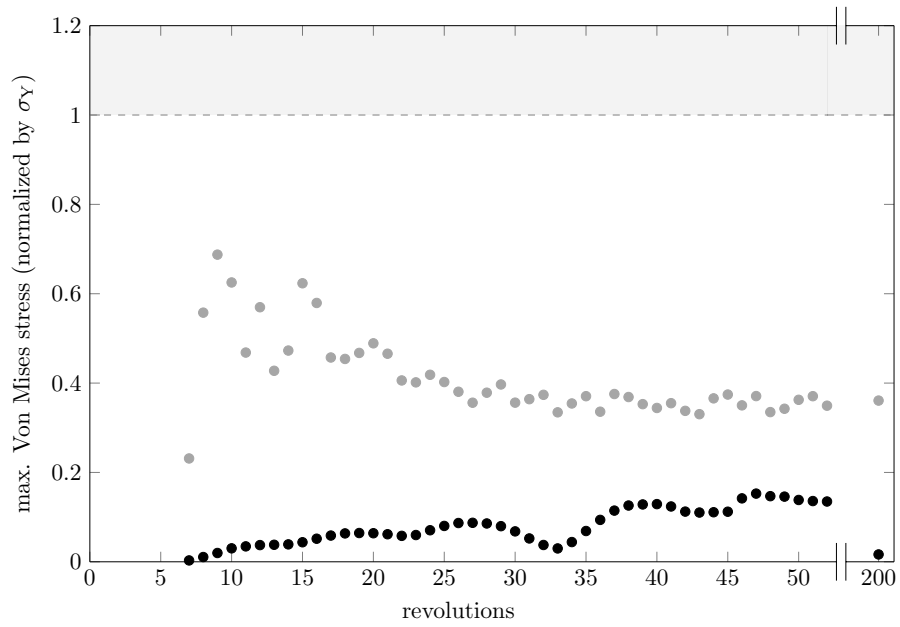


**Figure 12.** maximal Von Mises stresses at  $\Omega_N = 1800$  rad/s for the case with direct contact ( $\bullet$ ) and for the case with abrasion coating ( $\bullet$ );  $\sigma_Y = 1.38$  GPa

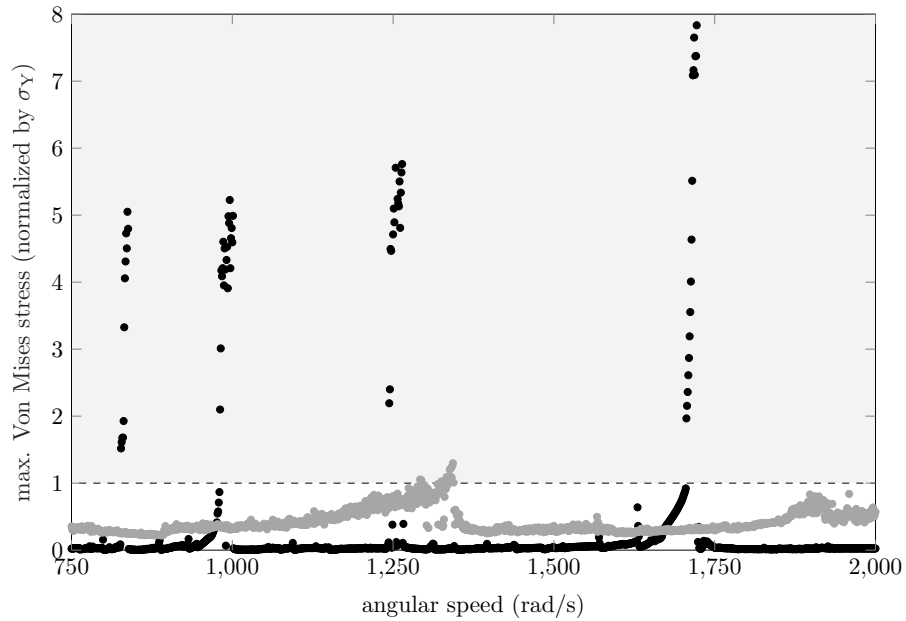


**Figure 13.** maximal Von Mises stresses over the last revolution at each angular speed for the case with direct contact ( $\bullet$ ) and for the case with abrasion coating ( $\bullet$ );  $\sigma_Y = 1.38$  GPa

view, the removal of the abradable coating changes the contact conditions and can lead to diverging interactions with increasing vibration amplitude and abradable wear, or a loss of contact and the end of vibrations. From an aerodynamics point of view, increased clearances may lead to increased aerodynamic losses and as such high levels of wear are not desirable.

The maximal level of wear over the casing circumference at the end of the simulation for each angular speed is presented in Fig. 14a. As could be anticipated, higher levels of wear are observed at the interactions which resulted in higher radial displacements. At these angular speeds, abradable coating is fully worn off at least at one position around the casing. The circumferential distribution of the zones of higher wear is analyzed by Fourier transform, as shown in Fig. 14b. Spatial frequencies are related to the number of privileged areas of wear around the casing. In particular, the larger level observed for the spatial frequency 0 denotes wear all around the casing. Important contributions are also observed for spatial frequencies 7, 6, 5 and 4 at the interactions with corresponding engine orders: if the blade vibration frequency is  $n$  times the rotation frequency, it will come back at the same radial position  $n$  times per revolution and will therefore impact the casing at  $n$  equally spaced positions and wear the abradable coating at these positions.

#### 5.4 Summary and discussion

These results demonstrate the relevance of the proposed test case to constitute a benchmark for blade/casing interactions. On one hand, the proposed test case allows observing typical phenomena of industrial blade/casing interactions:

**nonlinear behaviour:** simulated responses exhibit jumps with small variation of one operational parameter, and interaction speeds are increased by the contact stiffening phenomenon;

**beneficial effect of abradable coating:** a significant reduction in response amplitude is obtained at most angular speeds through abradable coating deposition on the casing;

**high-amplitude interactions:** in the case with abradable coating, interactions between the first bending mode and specific engine orders lead to high levels of vibration with full abradable removal over small angular speed ranges.

On the other hand, the employed numerical strategy, along with the realistic geometry of the blade, allow extracting a variety of quantities of interest that are relevant for both researchers and industrial designers. The presented results provide the three following types of information:

**identification of the angular speeds of high-amplitude interactions:** the rms level of displacement over a wide angular speed range allows obtaining interaction speeds that would be underestimated by using the Campbell diagram, and identify which of all the potential interactions actually lead to high-amplitude responses;

**assessment of the potential consequences of the interactions:** maximal stresses within the blade can be used to assess if an interaction represents a significant risk for the blade integrity; abradable wear at the end of the simulation also provide information on the modification of the blade/casing clearances following an interaction;

**analysis of the phenomena at stake:** the spectral maps and the frequency analysis of the abradable wear pattern provide information on the different modes involved in an interaction, as high-amplitude interactions may couple more than one mode.

Knowing the blade operating conditions, these results constitute a strong basis to assess its robustness to contact events, and to identify possible improvements in the blade design.

## 6 Effect of sweep and lean variations

### 6.1 Re-designed blades with sweep and lean variations

The geometry of the reference blade can be modified either by acting on the MCA parameters of each profile, or by modifying the stacking line along which the profiles are positioned by varying the sweep and lean of the blade. Previous works have shown that modifying the stacking line has significant consequences on the aerodynamic performances of the blade [31, 54, 55] as well as on the blade's response to contact events [38, 56]. Therefore, six

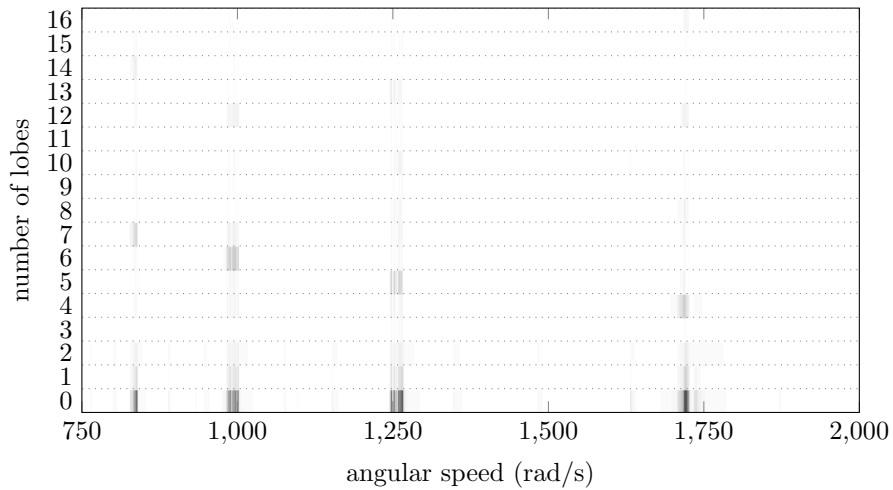
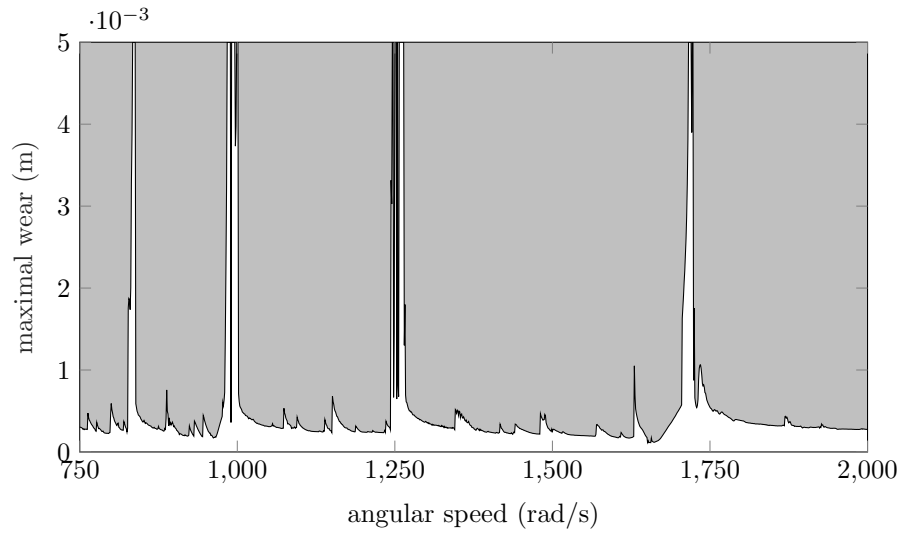


**Figure 14.** wear of the abradable coating at the end of the simulation for each angular speed: (a) maximal wear over the circumference and (b) spatial frequency content of the circumferential wear pattern

new blades are defined by varying the sweep and lean to compare their responses to contact events with that of the reference blade.

### 6.1.1 Sweep and lean definitions

Modification of the stacking line consists in translating the center of gravity of each profile. This translation is generally defined in two orthogonal directions, modification in one direction being called “sweep” while modification in the other direction is called “lean”. Different definitions of the sweep and lean can be found in the literature [31, 32, 54, 57], as described in Fig. 15: chordwise sweep (a) and dihedral or true lean (b) are defined based on the chordwise direction of each profile; axial sweep (c) and tangential lean (d) are defined based on the  $z$  and  $\theta$  directions in the cylindrical coordinate system of the profile. In the present paper, definitions (c) and (d) are used: axial sweep is defined as a displacement in the axial direction  $z^2$ ; tangential lean is defined as an angle between the centers of gravity of the new and original profiles, measured at the rotor axis.

### 6.1.2 Description of the six modified blades

In order to observe the effect of sweep and lean in the context of contact interactions, three types of stacking line modification are considered, based on the literature. The geometry of the reference blade is modified by choosing values for sweep and lean at four span values, and interpolating these values with a cubic B-spline to all 11 profile levels. For each stacking line modification, two blades are studied, one with 50% of the modification applied, and one with 100% of the modification applied. In total, six blades are thus compared to the reference blade:

**Forward-leaned blades:** blades  $L_{50}$  and  $L_{100}$  are based on a geometry proposed in [58]. The blades are leaned in the direction of rotor rotation on their outer half span, and slightly swept in the downstream direction on their inner half span. The exact parameter values are given in Tab. 4 and plotted in Fig. 16(a) and (b); Fig. 16(c) and (d) show the resulting 3D geometry. Biollo and Benini [2, 31, 58] showed that forward lean increased adiabatic efficiency by modifying the three-dimensional structure of the shock. The positive effect of forward lean on adiabatic efficiency was also observed by Ahn [32], though in this case smaller lean values than [58] were investigated. Indeed, large lean angles lead to higher stresses levels in the blade under centrifugal loads, due to higher bending loads. To mitigate this effect, Biollo [58] suggested adding a slight axial sweep on the blade’s inner half span in the downstream direction. The final geometry, studied in [58] and corresponding to blade  $L_{100}$ , leads to higher efficiency (0.8 percentage points at the peak efficiency condition), and similar total pressure ratio and choking mass flow compared to the original rotor 37.

**Backward-swept blades:** blades  $S_{50}$  and  $S_{100}$  are based on one of the blades studied in [31]. The exact parameter values are given in Tab. 4, and the corresponding axial sweep and (null) lean angle are plotted along with their effect on the blade geometry in Fig. 17. In [31], the backward-swept blade demonstrates a slightly higher efficiency and a higher choking mass flow, but the improvement is lower than the previously described forward-leaned blade.

<sup>2</sup>Note that in practice, sweep is applied as an angle in the algorithm described by Crouse [44] and used in the present work.

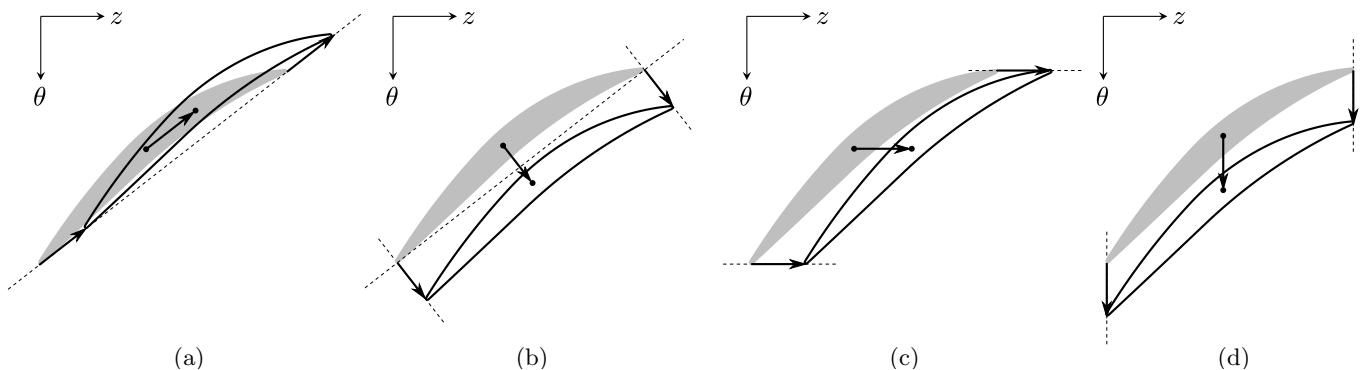


Figure 15. definitions of sweep and lean: (a) chordwise sweep, (b) dihedral/true lean, (c) axial sweep and (d) tangential lean

**Full forward chordwise swept blades:** blades CS<sub>50</sub> and CS<sub>100</sub> are based on a geometry proposed in [55] to reduce the sensitivity of the blade aerodynamic performances to tip clearance variations. Blade CS<sub>100</sub> corresponds to a 20° chordwise sweep as prescribed in [55], and blade CS<sub>50</sub> corresponds to a 10° chordwise sweep. The prescribed angle is measured in the chord direction between the centers of gravities of the profiles before and after modification, the reference being the center of gravity of the hub profile. Therefore, for a profile  $i$ , the corresponding axial sweep  $s_i$  and lean angle  $l_i$  are computed with the following expressions:

$$s_i = \tan \beta \times (r_i - r_0) \cos \left( \frac{y_{oc,i} - y_{ic,i}}{z_{oc,i} - z_{ic,i}} \right) \quad (11)$$

$$l_i = \arcsin \left( \tan \beta \times \frac{r_i - r_0}{r_i} \sin \left( \frac{y_{oc,i} - y_{ic,i}}{z_{oc,i} - z_{ic,i}} \right) \right) \quad (12)$$

where  $\beta$  is the applied chordwise angle,  $r_0$  and  $r_i$  are the radial position of the center of gravity for the hub profile and the  $i^{\text{th}}$  profile respectively, and  $y_{oc,i}$ ,  $y_{ic,i}$ ,  $z_{oc,i}$  and  $z_{ic,i}$  are the  $y$  and  $z$  coordinates of the outlet (o) and the inlet (i) on the centerline (c). The exact parameter values are given in Tab. 4, and the corresponding axial sweep and lean angle are plotted along with their effect on the blade geometry in Fig. 18.

### 6.1.3 Parameters of the simulations

The parameters are identical to those used for the reference blade (see section 4.5). In particular, the blade tip clearance is the same for all blades, 0.356 mm; the tip clearance is not modified by the sweep and lean variations, in order to compare only the blades' dynamics without modifying other parameters. This is consistent with studies on the aerodynamic behaviour of the blades [31], where the tip clearance as well as the position of the blade tip are kept constant when modifying the blade geometry.

## 6.2 Blade tip displacement

As for the reference blade, radial displacement at the leading edge of the blade tip is post-processed over the last 100 revolutions for blades L<sub>100</sub>, S<sub>100</sub> and CS<sub>100</sub>, and the corresponding spectral maps are presented in Fig. 19. All spectral maps are plotted with the same color code (same minimal and maximal values as for the reference blade Fig. 8), and the frequency of interaction between the first bending mode and engine order  $e_{o4}$ ,  $\Omega_{1B/e_{o4}}$ , is highlighted for each blade. Compared to the reference blade, L<sub>100</sub> leads to a similar map with slightly less visible interactions, S<sub>100</sub> leads to a dramatic reduction in the amplitudes of all interactions, and CS<sub>100</sub> leads to more zones of interactions, and to a wider angular speed range of interaction for interaction 1B/ $e_{o4}$ .

For a more quantitative analysis of the consequences of sweep and lean variations, the focus is made on the 1B/ $e_{o4}$  interaction. The radial displacement levels are presented in Fig. 20a, 20c and 20e, and tangential displacement levels are presented in Fig. 20b, 20d and 20f, for the leaned, swept and chordwise swept blades, respectively. For all blades, a clear change in the angular speed of the interaction is visible, as sweep and lean variations modify the natural frequencies of the blades. The interaction speeds are given for all blades in Tab. 5, with a comparison between the speeds predicted through the blades' Campbell diagram and the actual interaction frequency identified from radial displacement. As was observed for the reference blade, actual interaction speeds are higher than predicted because of the contact stiffening phenomenon. The amplitudes of radial and tangential displacements are also modified (Fig. 20). It is important to notice that, around the interaction, the levels of displacement computed for the last 100 revolutions are too large compared to the blade dimensions for the linear elastic hypotheses to be applicable: therefore, only significant trends are analyzed from these graphs. Blades L<sub>50</sub> and L<sub>100</sub>, see Figs. 20a and 20b, lead to slightly decreased radial displacements and slightly increased tangential displacements; overall, the behaviour is not significantly different from the reference blade. Blades S<sub>50</sub> and S<sub>100</sub>, see Figs. 20c and 20d, lead to a dramatic reduction of radial displacement, and a significant reduction of tangential displacement. Blades CS<sub>50</sub> and CS<sub>100</sub>, see Figs. 20e and 20f, lead to slightly increased radial and tangential displacements. Moreover, the width of the interaction peaks seem significantly larger for blades L<sub>50</sub>, CS<sub>50</sub> and CS<sub>100</sub> compared to the reference blade.

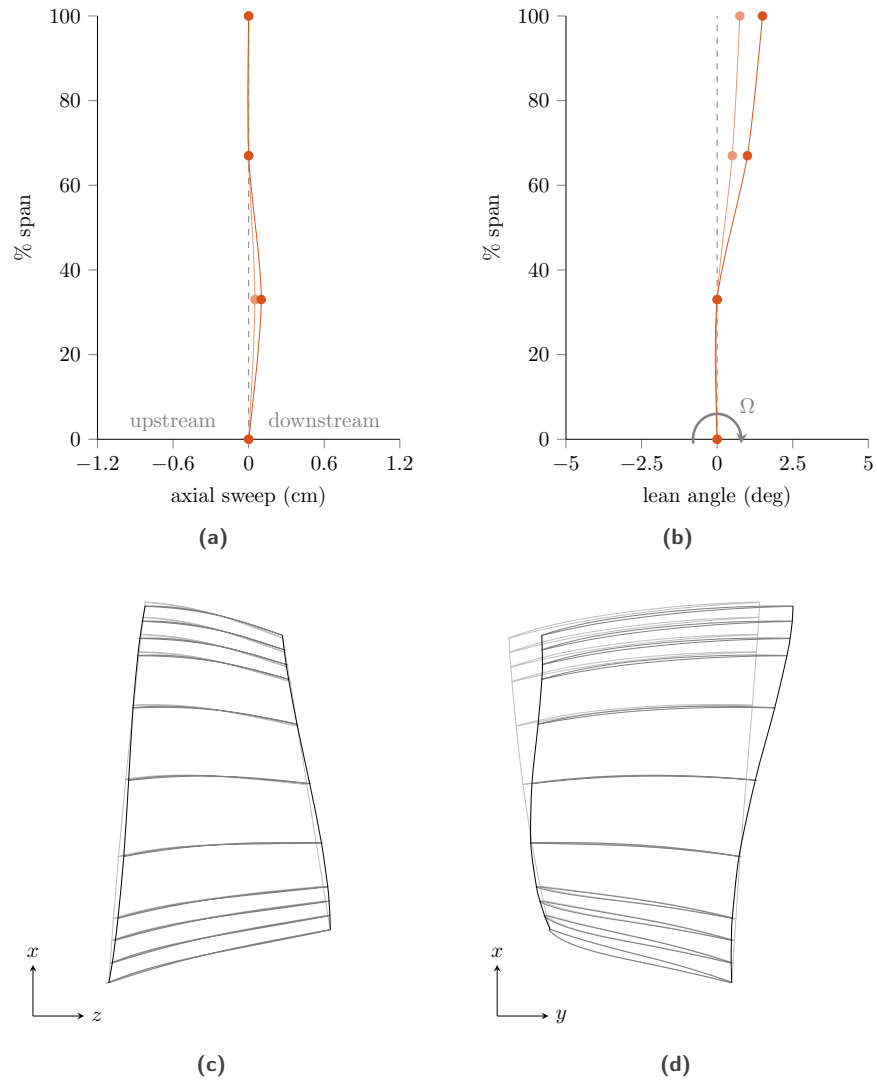


**Figure 16.** axial sweep and tangential lean applied to the forward-leaning blades: (a) sweep and (b) lean applied to the stacking line for blades L<sub>50</sub> and L<sub>100</sub>; (c) side view and (d) front view of the 3D geometry of L<sub>100</sub> blade (in black) compared to Ref blade (in light grey)

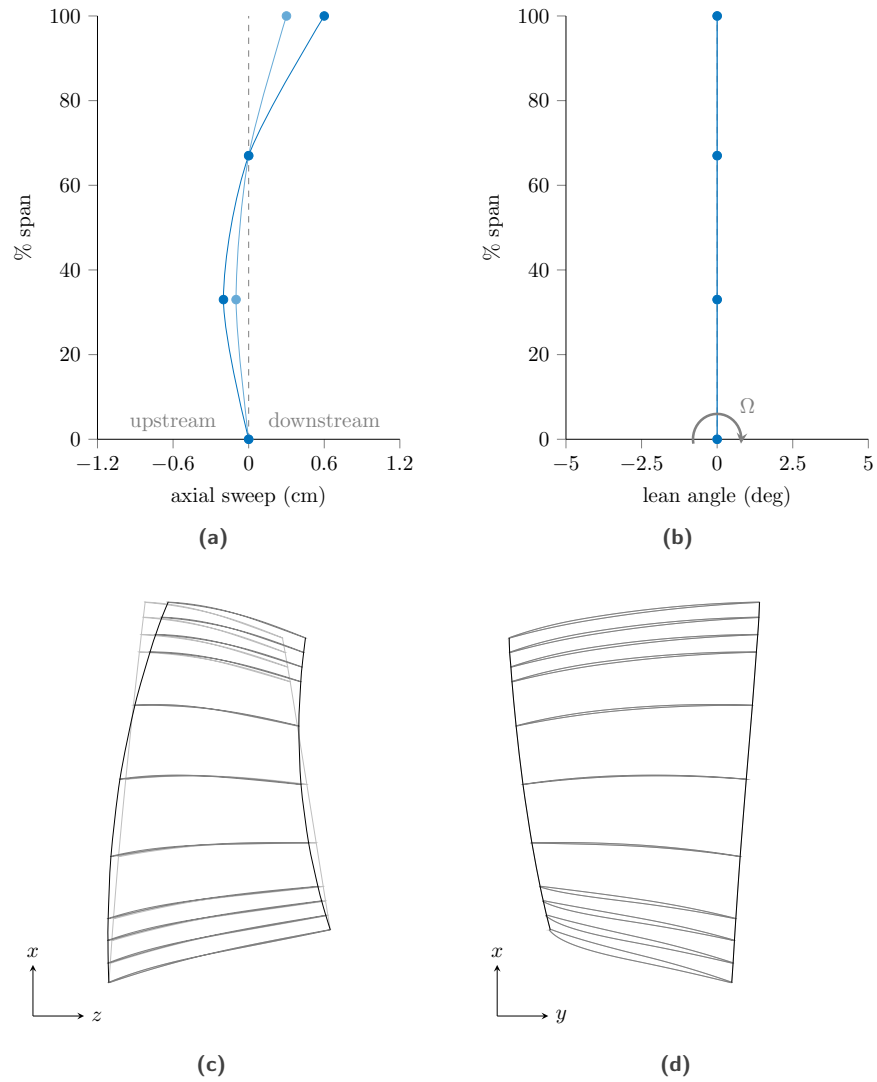


**Figure 17.** axial sweep and tangential lean applied to the backward-swept blades: (a) sweep and (b) lean applied to the stacking line for blades S<sub>50</sub> and S<sub>100</sub>; (c) side view and (d) front view of the 3D geometry of S<sub>100</sub> blade (in black) compared to Ref blade (in light grey)

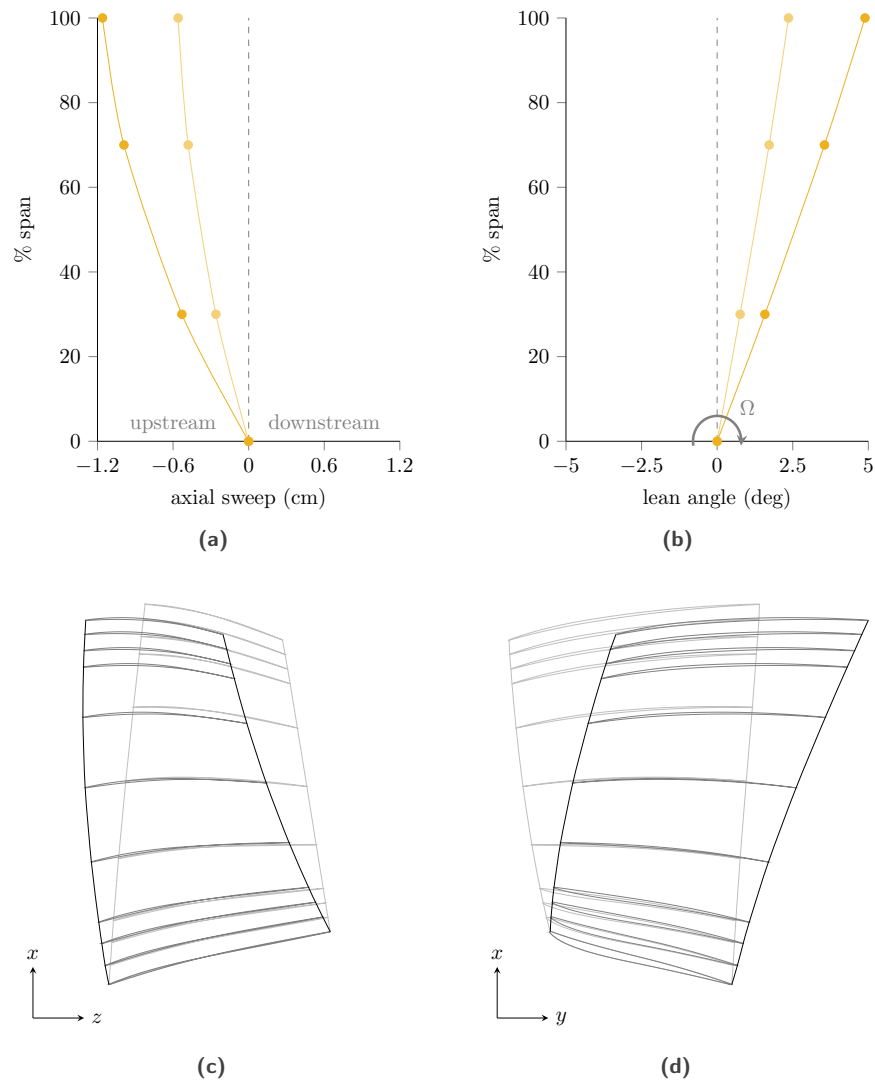


**Figure 18.** axial sweep and tangential lean applied to the full forward chordwise swept blades: (a) sweep and (b) lean applied to the stacking line for blades CS<sub>50</sub> and CS<sub>100</sub>; (c) side view and (d) front view of the 3D geometry of CS<sub>100</sub> blade (in black) compared to Ref blade (in light grey)

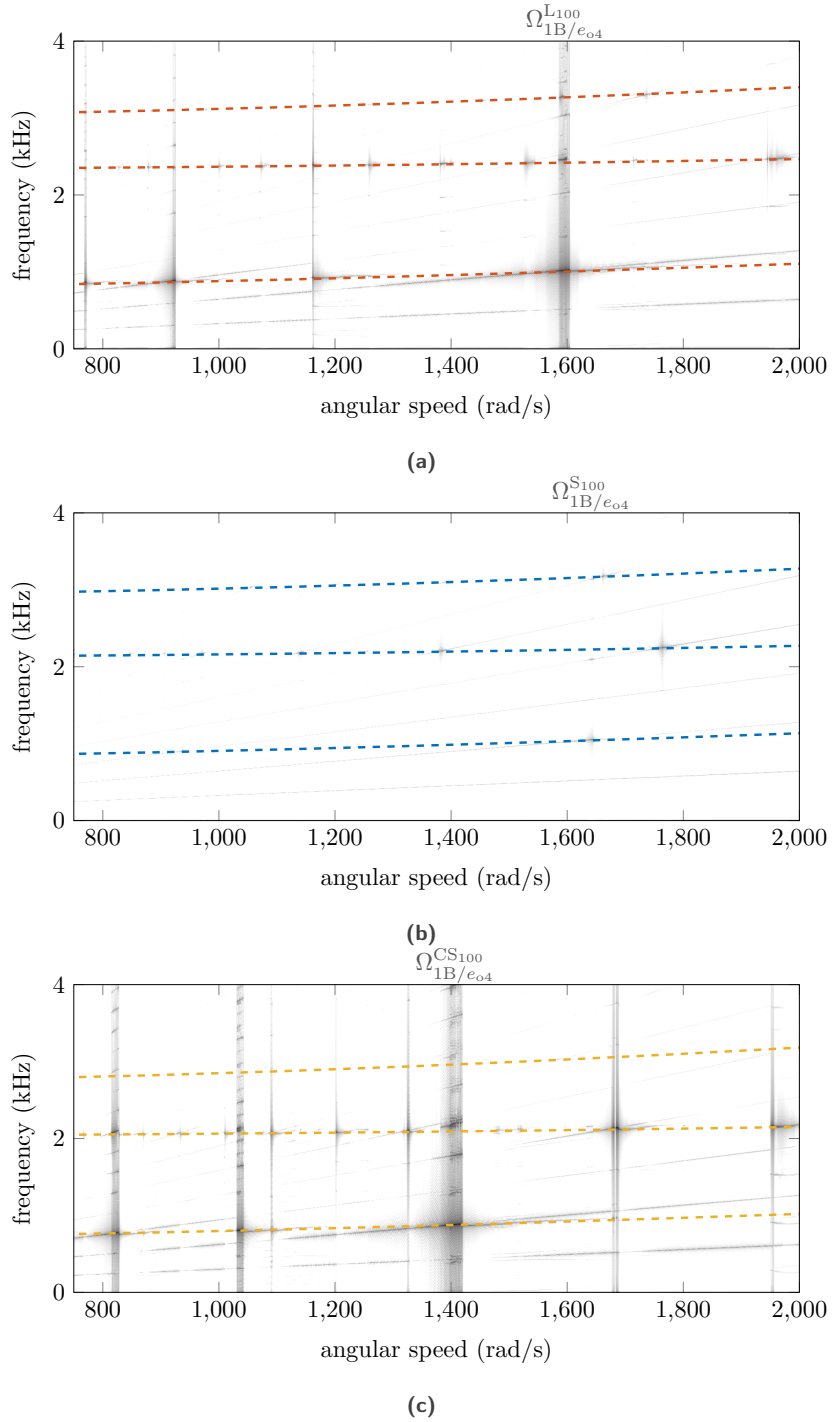


**Figure 19.** spectral maps of the radial displacement: (a) blade  $L_{100}$  (forward lean), (b) blade  $S_{100}$  (backward sweep) and (c) blade  $CS_{100}$  (full forward chordwise sweep)

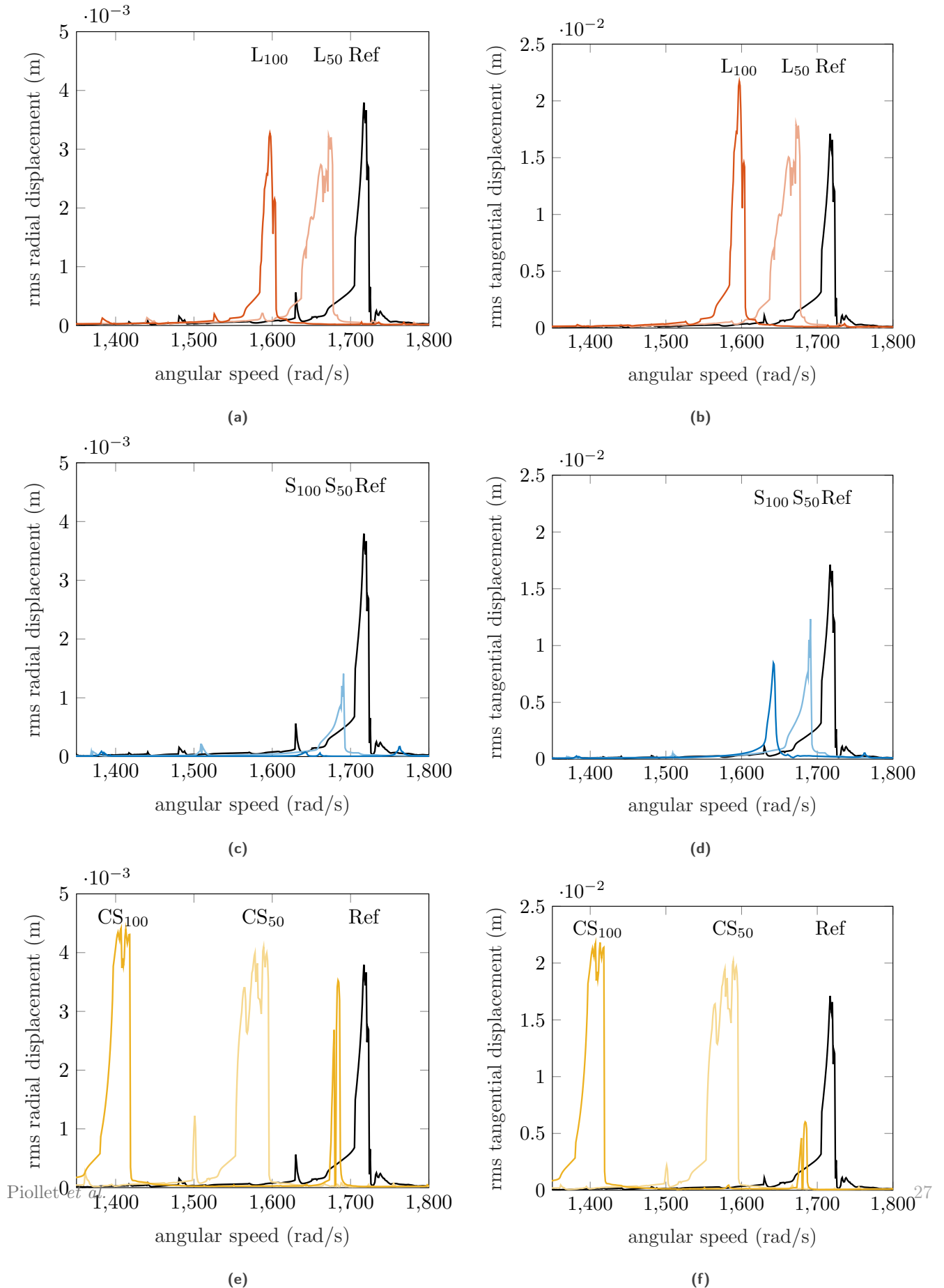


Figure 20. root-mean-square displacement levels for sweep and lean variations: (a) radial and (b) tangential, blades Ref, L<sub>50</sub>

	% span	50%		100%	
		sweep (cm)	lean (deg)	sweep (cm)	lean (deg)
L	100	0.00	0.75	0.00	1.50
	67	0.00	0.50	0.00	1.00
	33	0.05	0.00	0.10	0.00
	0	0.00	0.00	0.00	0.00
S	100	0.30	0.00	0.60	0.00
	67	0.00	0.00	0.00	0.00
	33	-0.10	0.00	-0.20	0.00
	0	0.00	0.00	0.00	0.00
CS	100	-0.56	2.37	-1.16	4.89
	70	-0.48	1.72	-0.99	3.56
	30	-0.26	0.76	-0.53	1.58
	0	0.00	0.00	0.00	0.00

**Table 4.** applied sweep and lean for forward leaned (L), backward swept (S) and full forward chordwise swept (CS) blades

	50%		100%	
	Campbell	max. rms	Campbell	max. rms
$\Omega_{1B/e_{o4}}^L$ (rad/s)	1621	1672	1564	1597
$\Omega_{1B/e_{o4}}^S$ (rad/s)	1660	1691	1635	1642
$\Omega_{1B/e_{o4}}^{CS}$ (rad/s)	1532	1589	1362	1407

**Table 5.** interaction speeds corresponding to the  $1B/e_{o4}$  intersection, obtained from the Campbell diagrams and from the speed at maximal radial displacement for forward leaned (L), backward swept (S) and full forward chordwise swept (CS) blades

### 6.3 Dynamic clearance

Previous works have shown a relationship between a blade’s robustness to contact events and its dynamic clearance, studied in details in [56] and investigated previously as the “clearance consumption” in [59]. The dynamic clearance quantifies the variation of the radial position of a given point on the blade tip as the blade vibrates along one of its free-vibration modes: large dynamic clearance means that vibration along the mode modifies significantly the blade/casing clearance. Designing blades with reduced dynamic clearances on one or more of their modes is one avenue currently investigated to design blades robust to contact interactions [56].

For all seven blades, the dynamic clearance  $c_d$  at the leading edge is plotted in Figs. 21 and 22 against the corresponding tangential displacement  $\mathbf{u}_\theta^{LE}$  for the first bending mode and the first torsion mode, respectively. The important information in these graphs is the slope of the dynamic clearance for each blade: reducing the slope means that for the same tangential displacement, clearance at the leading edge will vary less. For the first bending mode (Fig. 21), blades  $L_{50}$  and  $L_{100}$  lead to a slightly smaller dynamic clearance than the reference blade,  $S_{50}$  and  $S_{100}$  lead to a significantly smaller dynamic clearance, and  $CS_{50}$  and  $CS_{100}$  lead to a slightly larger dynamic clearance. For the first torsion mode (Fig. 22), blades  $L_{50}$  and  $L_{100}$  also lead to a slightly smaller dynamic clearance than the reference blade,  $S_{50}$  and  $S_{100}$  lead to a dramatic reduction in dynamic clearance, and  $CS_{50}$  and  $CS_{100}$  exhibit the same dynamic clearance as the reference blade. These observations are consistent with previous studies showing that smaller dynamic clearance is related to lower blade’s responses to contact events [59], as  $S_{50}$  and  $S_{100}$  exhibit the largest decrease in dynamic clearance as well as the lowest radial and tangential displacements. It is important to note, however, that the reduction is particularly striking for the first torsion mode, while interactions seem to occur mainly with the first bending mode. This confirms recent results showing that an efficient improvement of the blade’s robustness may involve taking into account the dynamic clearance of more modes than only the first bending mode [56].

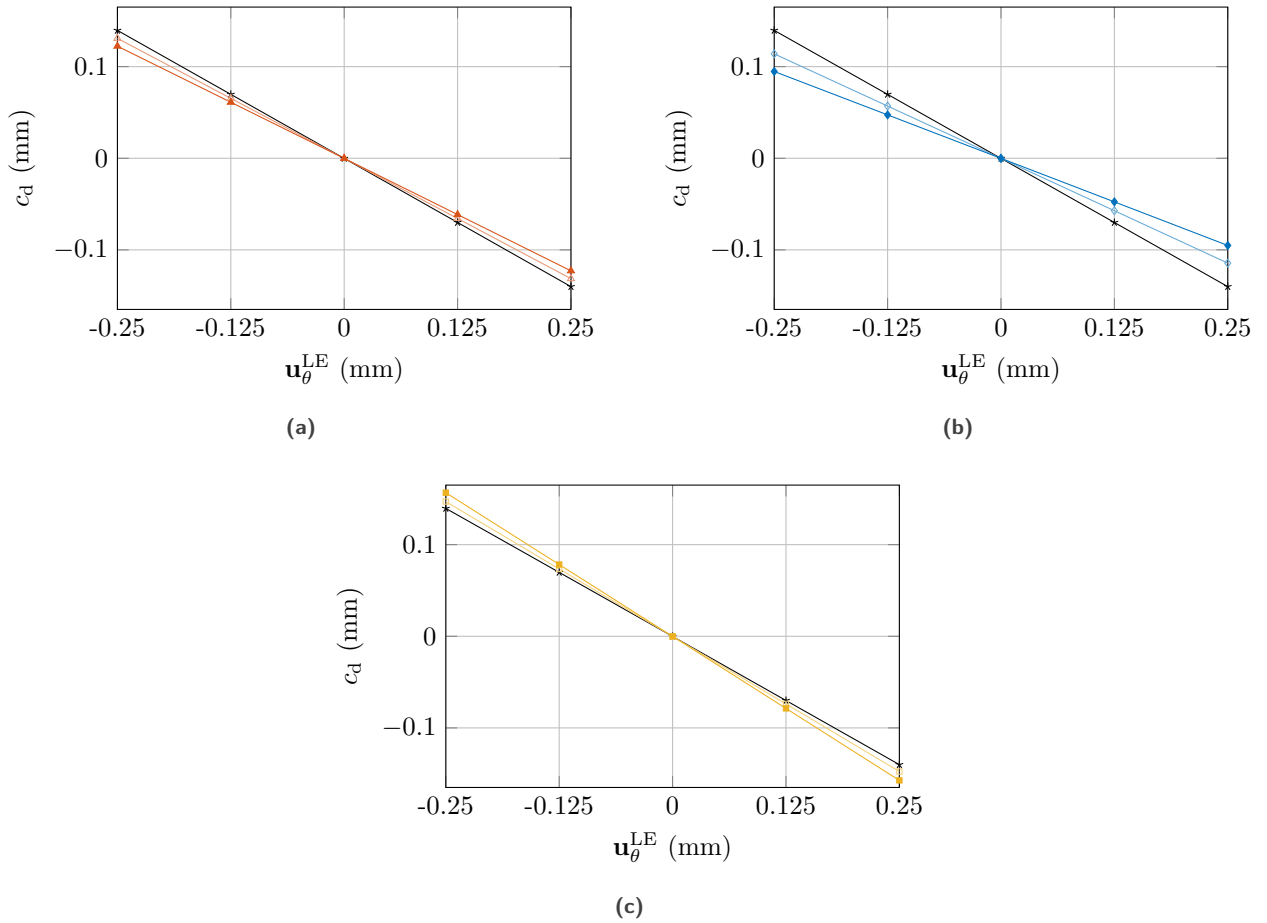


**Figure 21.** dynamic clearances for the first bending mode: (a) blades Ref, L<sub>50</sub> and L<sub>100</sub>; (b) blades Ref, S<sub>50</sub> and S<sub>100</sub>; blades Ref, CS<sub>50</sub> and CS<sub>100</sub>

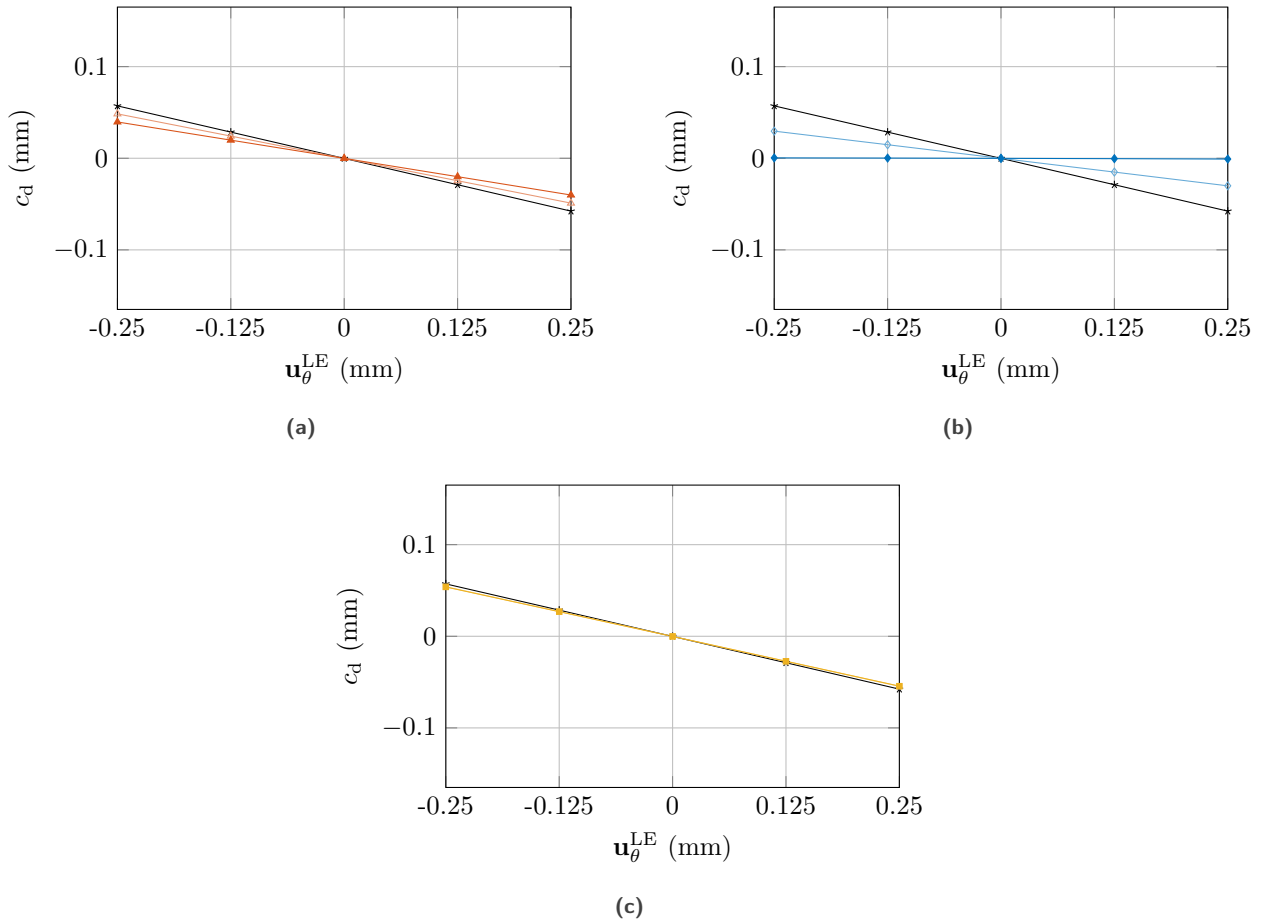


**Figure 22.** dynamic clearances for the first torsion mode: (a) blades Ref, L<sub>50</sub> and L<sub>100</sub>; (b) blades Ref, S<sub>50</sub> and S<sub>100</sub>; (c) blades Ref, CS<sub>50</sub> and CS<sub>100</sub>

## 6.4 Von Mises stress

Maximal Von Mises stresses within the modified blades are computed on submeshes defined with the same constraints as described in section 5.2.1. The maximal stresses within blades  $L_{100}$ ,  $S_{100}$  and  $CS_{100}$  are plotted on Fig. 23 over the first revolutions at their  $1B/e_{o4}$  interaction speeds (see Tab 5). Maximal stress within the reference blade exceeds the blade's yield stress earlier than for the modified blades, and is higher at the end of the simulation than within the other blades, which seems to indicate that the modifications of the blades improve their robustness to contact events. In particular, maximal stress within blade  $CS_{100}$  exceeds the yield stress during the 78<sup>th</sup> revolution, which is significantly later than for the other blades: yield stress is exceeded during the 40<sup>th</sup>, 44<sup>th</sup> and 51<sup>st</sup> revolution for the reference blade, blade  $S_{100}$  and blade  $L_{100}$  respectively. On the other hand, blade  $S_{100}$  exhibit the lowest maximal Von Mises stress at the end of the simulation, more than three times lower than the reference blade.

Analysis at one angular speed is not sufficient to assess the robustness of the blade to contact event. In particular, angular speed may vary during acceleration or deceleration phases. Though variable angular speed simulations are beyond the scope of the present article, the risk of initiating large vibrations when crossing an interaction is here assessed from the width of the angular speed range over which the blade's yield stress is exceeded due to the interaction. The maximal Von Mises stresses are computed over the last revolution for the six modified blades around interaction  $1B/e_{o4}$ , and are presented on Fig. 24 along with the stress within the reference blade. The width of the angular speed range over which stresses exceed the yield stress within the reference blade is  $w_{1B/e_{o4}}^{Ref} = 17$  rad/s. Forward-leaned blades lead to increasing then decreasing width,  $w_{1B/e_{o4}}^{L50} = 40$  rad/s and  $w_{1B/e_{o4}}^{L100} = 19$  rad/s: as was observed with other quantities, blade  $L_{100}$  has a behaviour similar to the reference blade. Backward-swept blades  $S_{50}$  and  $S_{100}$  lead respectively to a similar and significantly reduced width:  $w_{1B/e_{o4}}^{S50} = 16$  rad/s and  $w_{1B/e_{o4}}^{S100} = 8$  rad/s. Full forward chordwise swept blades  $CS_{50}$  and  $CS_{100}$  lead to a significant increase in the angular speed range of interaction:  $w_{1B/e_{o4}}^{CS50} = 42$  rad/s and  $w_{1B/e_{o4}}^{CS100} = 32$  rad/s.

## 6.5 Discussion

The analysis of the six modified blades can serve as a basis to discuss two important points regarding blade design for robustness to contact events: on one hand, the definition of relevant criteria to assess the blade's robustness; on the other hand, guidelines regarding the type of stacking line modifications that are beneficial or detrimental to the blade's robustness.

When assessing the consequences of geometry modifications on a blade's robustness, displacement at the blade tip is a natural criterion as it is directly related to the contact region; however, this local quantity is not sufficient to assess the risk of blade failure. In terms of blade durability, the maximal stress within the blade during contact interactions is a critical quantity, and two criteria have been considered: the time for which yield stress is first exceeded, and the width of the angular speed range over which yield stress is exceeded. The width of interaction seems the most relevant criterion: indeed, a wide angular speed range of interaction increases the risk of encountering the interaction, and during a constant acceleration it increases the time spent at a critical angular speed. As stress is less straightforward to compute than displacement as the outcome of a simulation, it can be observed that the tangential displacement (Fig. 20) carries similar information on the width of the interaction, minus the notion of yield stress, and therefore may serve as a first assessment of the blade's robustness. Finally, the dynamic clearance is a criterion that can be obtained through a short static computation, and as such it constitutes a good first criterion to evaluate the consequences of a blade modification before performing a full contact simulation.

Based on these criteria, for interaction  $1B/e_{o4}$  and under the assumptions of the employed numerical strategy, the following guidelines can be formulated from the behaviour of blades  $L_{100}$ ,  $S_{100}$  and  $CS_{100}$ :

**Forward-leaned blades:** the behaviour of blade  $L_{100}$  is similar to that of the reference blade in terms of the level of radial and tangential displacements, the number of revolutions before exceeding yield stress, and the angular speed range over which yield stress is exceeded. In this sense, it may constitute a good compromise to improve the aerodynamic performances without deteriorating the robustness to contact. However, the robustness of the reference blade may not be sufficient and in this case an improvement of the robustness may be desirable.

**Backward swept blades:** blade  $S_{100}$  leads to a significant improvement in the blade's robustness as assessed by most criteria; displacement at the blade tip and stress within the blade are significantly reduced, and the width of interaction is half of the width for the reference blade. Dynamic clearance is lower for both the first

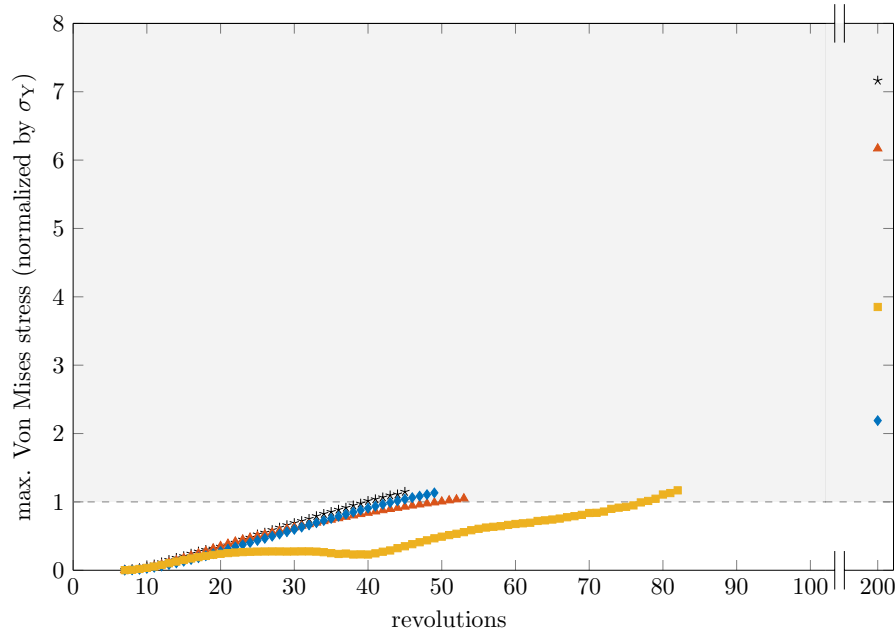


**Figure 23.** maximal Von Mises stresses within the reference blade at  $\Omega_{1B/e_{o4}}^{\text{Ref}} = 1717$  rad/s ( $\star$ ), blade  $L_{100}$  at  $\Omega_{1B/e_{o4}}^{L100} = 1597$  rad/s ( $\blacktriangle$ ), blade  $S_{100}$  at  $\Omega_{1B/e_{o4}}^{S100} = 1642$  rad/s ( $\blacklozenge$ ) and blade  $CS_{100}$  at  $\Omega_{1B/e_{o4}}^{CS100} = 1407$  rad/s ( $\blacksquare$ )

bending mode and the first torsion mode. This blade also leads to the smallest modification of the blade’s resonance frequencies and interaction speeds, which may be interesting from a design point of view. The only criterion that is not significantly improved with this blade is the number of revolutions before exceeding the yield stress.

**Full forward chordwise swept blades:** the addition of full forward chordwise sweep is the modification that seems the most detrimental to the blade’s robustness to contact events. Both displacement amplitudes and width of interaction show a significantly less robust behaviour for blade  $CS_{100}$  than for the reference blade. On the other hand, stress within this blade takes almost twice the number of revolutions to exceed yield stress compared to the reference blade, which may be interesting in specific situations, and may necessitate further investigation.

These guidelines based on blades  $L_{100}$ ,  $S_{100}$  and  $CS_{100}$  are partially confirmed by the results obtained for blades  $L_{50}$ ,  $S_{50}$  and  $CS_{50}$ . The 50% and 100% modifications generally demonstrate a continuity in their consequences compared to the reference blade in terms of displacement amplitude, dynamic clearance and interaction speeds. On the other hand, the width of the interaction does not show such continuity between the reference, 50% and 100% modifications.

## 7 Conclusions

In this paper, a reference blade geometry is proposed to serve as a benchmark for numerical simulations of blade/casing rubbing events. The geometry is based on the widely used aerodynamic test case NASA rotor 37 and detailed geometry parameters are provided.

The first objective of this benchmark is to serve as a basis for comparisons between existing numerical strategies. Simulations of response to contact events are performed for constant angular speeds on a wide angular speed range with time integration. All simulation parameters are provided. A variety of results are presented to give a clear picture of the blade behaviour: radial displacement, stress within the blade and wear of abradable coating. The effect of abradable coating is clearly highlighted: at most angular frequencies, displacement and stress are reduced

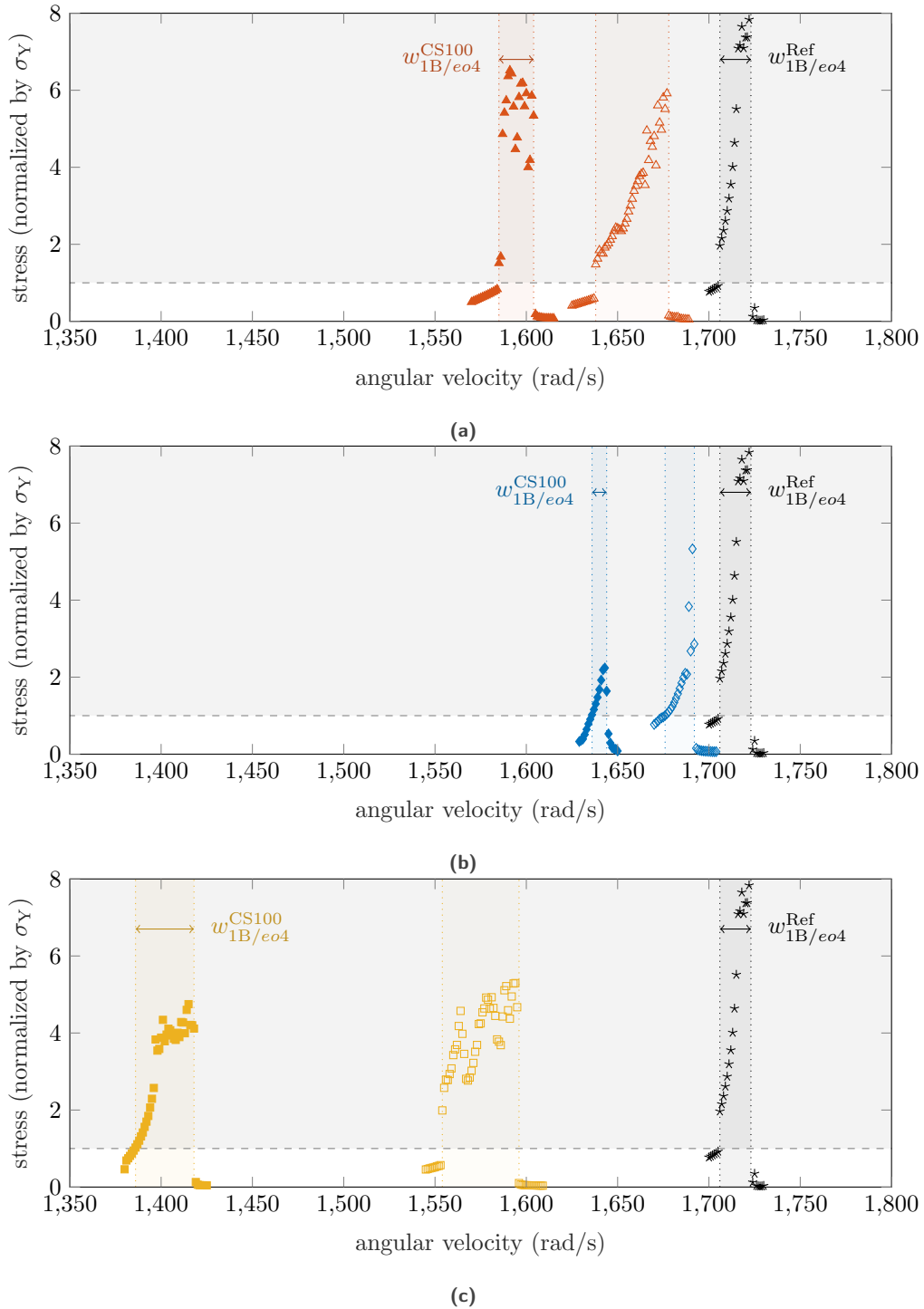


**Figure 24.** width of the interaction speed ranges over which yield stress is exceeded: (a) blades Ref, L<sub>50</sub> and L<sub>100</sub>; (b) blades Ref, S<sub>50</sub> and S<sub>100</sub>; (c) blades Ref, CS<sub>50</sub> and CS<sub>100</sub>

compared to direct blade/casing contact, but at specific angular speeds high amplitude interactions are observed, especially at intersections between engine orders and the first bending mode. This study shows that the proposed test case allows observing realistic responses to contact.

The second objective of this benchmark is to define guidelines for the design of blades that are robust to contact events. Previously published aerodynamic recommendations on sweep and lean variations are investigated in terms of their consequences on the blade's robustness to contact. Two types of modifications are identified as potentially interesting compromises: on one hand, a forward-leaned blade identified as very beneficial in terms of aerodynamic performances is shown to exhibit a similar robustness to contact events compared to the reference blade; on the other hand, a backward-swept blade identified as slightly beneficial in terms of aerodynamic performances is shown to represent a significant improvement in terms of robustness to contact events. In both cases, objectives of aerodynamic performances and robustness to contact events are not in contradiction with each other. On the contrary, a full forward chordwise swept blade identified as beneficial in terms of aerodynamic robustness is shown to exhibit a deteriorated robustness to contact events. A variety of physical quantities are compared for all studied blades; in particular, the width of the angular speed range over which an interaction occurs seems to be particularly well suited to compare the robustness of different blades. Other quantities that are less costly to obtain are also identified as relevant to assess the blade's robustness: tangential displacement also shows the width of the interactions, and dynamic clearance can serve as a simple criterion computed at low cost before performing advanced simulations.

In the end, this benchmark paves the way for comparisons between numerical strategies on a large variety of relevant mechanical results, and for future systematic investigations of the consequences of design modifications on blade's robustness to contact.

## Acknowledgment

This research was supported by the Natural Sciences and Engineering Research Council of Canada (NSERC) and the Fonds de Recherche du Québec - Nature et Technologies (FRQ-NT).

## References

- [1] T. Korakianitis, I. Hamakhan, M. Rezaenia, A. Wheeler, E. Avital, J. Williams, Design of high-efficiency turbomachinery blades for energy conversion devices with the three-dimensional prescribed surface curvature distribution blade design (CIRCLE) method, *Applied Energy* 89 (1) (2012) 215–227, doi: 10.1016/j.apenergy.2011.07.004.
- [2] E. Benini, Three-dimensional multi-objective design optimization of a transonic compressor rotor, *J. Propul. Power* 20 (3) (2004) 559–565, doi: 10.2514/6.2003-4090.
- [3] Australian Transport Safety Bureau, In-flight engine failure Sydney 03 February 2007 : Boeing Company 747-438, VH-OJM, Tech. rep., Australian Transport Safety Bureau (2008).  
URL [https://www.atsb.gov.au/publications/investigation\\_reports/2007/aair/aair200700356/](https://www.atsb.gov.au/publications/investigation_reports/2007/aair/aair200700356/)
- [4] A. Millecamps, J. Brunel, P. Dufrénoy, F. Garcin, M. Nucci, Influence of thermal effects during blade-casing contact experiments, in: *Proceedings of the ASME 2009 IDETC & CIE conference*, ASME, 2009, pp. 855–862, doi: 10.1115/DETC2009-86842 - oai: hal-01223060.
- [5] K. E. Turner, M. Dunn, C. Padova, Airfoil deflection characteristics during rub events, *Journal of Turbomachinery* 134 (2012) 011018–1–8, doi: 10.1115/gt2010-22166.
- [6] S. K. Sinha, Non-linear dynamic response of a rotating radial timoshenko beam with periodic pulse loading at the free end, *International Journal of Non-Linear Mechanics* 40 (2005) 113–149, doi: 10.1016/j.ijnonlinmec.2004.05.019.
- [7] P. Schmiechen, Travelling wave speed coincidence, Ph.D. thesis, Imperial College of Science, Technology and Medicine - University of London, London, England (1997).
- [8] A. Batailly, M. Legrand, P. Cartraud, C. Pierre, Assessment of reduced models for the detection of modal interaction through rotor stator contacts, *Journal of Sound and Vibration* 329 (2010) 5546–5562, doi: 10.1016/j.jsv.2010.07.018 - oai: hal-00660863.

- [9] A. Muszynska, Whirl and whip-rotor/bearing stability problems, *Journal of Sound and vibration* 110 (3) (1986) 443–462, doi: 10.1016/S0022-460X(86)80146-8.
- [10] S. K. Sinha, Rotordynamic analysis of asymmetric turbofan rotor due to fan blade-loss event with contact-impact rub loads, *Journal of Sound and Vibration* 332 (9) (2013) 2253 – 2283, doi: 10.1016/j.jsv.2012.11.033.
- [11] N. Salvat, A. Batailly, M. Legrand, Two-dimensional modeling of shaft precessional motions induced by blade/casing unilateral contact in aircraft engines, in: *Proceedings of the ASME Turbo Expo 2014, Dusseldorf, Germany, 2014*, p. V07BT33A011, GT2014-25688.
- [12] M. Parent, F. Thouverez, F. Chevillot, Whole engine interaction in a bladed rotor-to-stator contact, in: *Proceedings of the ASME Turbo Expo 2014, Dusseldorf, Germany, 2014*, p. V07AT31A003, GT2014-25253.
- [13] M. Borel, A. Nicoll, H. Schlapfer, R. Schmid, The wear mechanisms occurring in abradable seals of gas turbines, *Surface & Coatings Technology* 39 (1989) 117–126, doi: 10.1016/0257-8972(89)90046-7.
- [14] C. Padova, M. G. Dunn, J. Barton, K. Turner, A. Turner, D. DiTommaso, Casing treatment and blade-tip configuration effects on controlled gas turbine blade tip/shroud rubs at engine conditions, *Journal of Turbomachinery* 133 (1) (2011) 011016, doi: 10.1115/1.4000539.
- [15] R. Mandard, J.-F. Witz, X. Boidin, J. Fabis, Y. Desplanques, J. Meriaux, Interacting force estimation during blade/seal rubs, *Tribology International* 82 (2015) 504–513, doi: 10.1016/j.triboint.2014.01.026 - oai: hal-01166811.
- [16] G. Jacquet-Richardet, M. Torkhani, P. Cartraud, F. Thouverez, T. N. Baranger, M. Herran, C. Gibert, S. Baguet, P. Almeida, L. Peletan, Rotor to stator contacts in turbomachines. Review and application, *Mechanical Systems and Signal Processing* 40 (2) (2013) 401–420, doi: 10.1016/j.ymssp.2013.05.010 - oai: hal-00934050.
- [17] R. J. Williams, Simulation of blade casing interaction phenomena in gas turbines resulting from heavy tip rubs using an implicit time marching method, in: *Proceedings of the ASME Turbo Expo 2011 conference, GT2011-45495, Vancouver, Canada, 2011*, pp. 1007–1016, GT2011-45495.
- [18] E. Petrov, Multiharmonic analysis of nonlinear whole engine dynamics with bladed disc-casing rubbing contacts, in: *ASME Turbo Expo 2012: Turbine Technical Conference and Exposition, 2012*, pp. 1181–1191, GT2012-68474.
- [19] S. Nitschke, T. Wollmann, C. Ebert, T. Behnisch, A. Langkamp, T. Lang, E. Johann, M. Gude, An advanced experimental method and test rig concept for investigating the dynamic blade-tip/casing interactions under engine-like mechanical conditions, *Wear* doi: 10.1016/j.wear.2018.12.072.
- [20] P. Almeida, C. Gibert, F. Thouverez, X. Leblanc, J.-P. Ousty, Experimental analysis of dynamic interaction between a centrifugal compressor and its casing, in: *Proceedings of the ASME Turbo Expo 2014, Dusseldorf, Germany, 2014*, p. V07BT33A003, GT2014-25223.
- [21] H. Ma, D. Wang, X. Tai, B. Wen, Vibration response analysis of blade-disk dovetail structure under blade tip rubbing condition, *Journal of Vibration and Control* doi: 10.1177/1077546315575835.
- [22] H. Yuan, H. Kou, Compact-impact analysis of a rotating geometric nonlinear plate under thermal shock, *Journal of Engineering Mathematics* 90 (1) (2014) 119–140, doi: 10.1007/s10665-014-9727-0.
- [23] M. Legrand, C. Pierre, P. Cartraud, J. P. Lombard, Two-dimensional modeling of an aircraft engine structural bladed disk-casing modal interaction, *Journal of Sound and Vibration* 319 (1-2) (2009) 366–391, doi: 10.1016/j.jsv.2008.06.019 - oai: hal-00328186v2.
- [24] D. Arzina, Vibration analysis of compressor blade tip-rubbing, Master’s thesis, Cranfield University (2011).
- [25] G. Von Groll, D. Ewins, The harmonic balance method with arc-length continuation in rotor/stator contact problems, *Journal of Sound and Vibration* 241 (2) (2001) 223–233, doi: 10.1006/jsvi.2000.3298.
- [26] L. Peletan, S. Baguet, M. Torkhani, G. Jacquet-Richardet, Quasi-periodic harmonic balance method for rubbing self-induced vibrations in rotor–stator dynamics, *Nonlinear Dynamics* 78 (4) (2014) 2501–2515, doi: 10.1007/s11071-014-1606-8.

- [27] N. Carpenter, R. Taylor, M. Katona, Lagrange constraints for transient finite element surface contact, *International Journal for Numerical Methods in Engineering* 32 (1991) 103–128, doi: 10.1002/nme.1620320107.
- [28] A. Batailly, M. Legrand, Unilateral contact induced blade/casing vibratory interactions in impellers: analysis for flexible casings with friction and abradable coating, *Journal of Sound and Vibration* 348 (2015) 344–364, doi: 10.1016/j.jsv.2015.03.027 - oai: hal-01223575.
- [29] P. Almeida, C. Gibert, F. Thouverez, J.-P. Ousty, Numerical analysis of bladed disk-casing contact with friction and wear, in: *Proceedings of the ASME Turbo Expo 2015*, Montréal, Canada, 2015, p. V07BT32A026, GT2015-43435.
- [30] A. Ameri, Nasa rotor 37 CFD code validation glenn-ht code, in: *47th AIAA Aerospace Sciences Meeting including The New Horizons Forum and Aerospace Exposition*, 2009, p. 1060, doi: 10.2514/6.2009-1060.
- [31] E. Benini, R. Biollo, Aerodynamics of swept and leaned transonic compressor-rotors, *Applied Energy* 84 (10) (2007) 1012–1027, doi: 10.1016/j.apenergy.2007.03.003.
- [32] C.-S. Ahn, K.-Y. Kim, Aerodynamic design optimization of an axial flow compressor rotor, in: *ASME Turbo Expo 2002: Power for Land, Sea, and Air*, Amsterdam, The Netherlands, 2002, pp. 813–819, GT2002-30445.
- [33] Z. Burton, Analysis of low pressure steam turbine diffuser and exhaust hood systems, Ph.D. thesis, Durham University (2014).
- [34] D. Qi, Establishment of an open 3D steam turbine flutter test case, Master’s thesis, KTH (2016).
- [35] J. Little, Academic blade geometries for baseline comparisons of forced vibration response predictions, Master’s thesis, University of Central Florida (2017).
- [36] E. Piollet, A. Batailly, A program to compute compressor blade geometries from multiple-circular-arc parameters with sweep and lean (v1.0), oai: hal-02127993 (2019).
- [37] A. Batailly, Q. Agrapart, A. Millecamps, J.-F. Brunel, Experimental and numerical simulation of a rotor/stator interaction event within an industrial high-pressure compressor, *Journal of Sound and Vibration* 375 (2016) 308–331, doi: 10.1016/j.jsv.2016.03.016 - oai: hal-01342401.
- [38] A. Batailly, M. Legrand, A. Millecamps, F. Garcin, Numerical-experimental comparison in the simulation of rotor/stator interaction through blade-tip/abradable coating contact, *Journal of Engineering for Gas Turbines and Power* 134 (8) (2012) 082504–1–11, doi: 10.1115/1.4006446 - oai: hal-00746632.
- [39] L. Reid, R. D. Moore, Design and overall performance of four highly loaded, high-speed inlet stages for and advanced high-pressure-ratio core compressor, Tech. Rep. NASA TP-1337, NASA Lewis Research Center (1978).
- [40] J. Denton, Lessons from rotor 37, *Journal of Thermal Science* 6 (1) (1997) 1–13, doi: 10.1007/s11630-997-0010-9.
- [41] W. Cui, X. Xiang, Q. Zhao, J. Xu, The effect of sweep on flowfields of a highly loaded transonic rotor, *Aerospace Science and Technology* 58 (2016) 71–81, doi: 10.1016/j.ast.2016.08.002.
- [42] D. Hubler, Rotor 37 and stator 37 assembly (series: Photographs relating to agency activities, facilities and personnel, 1973 - 2013) (1977).  
URL <https://catalog.archives.gov/id/17468361>
- [43] R. D. Moore, L. Reid, Performance of single-stage axial-flow transonic compressor with rotor and stator aspect ratios of 1.19 and 1.26, respectively, and with design pressure ratio of 1.82, Tech. rep., NASA Lewis Research Center (1980).
- [44] J. E. Crouse, D. C. Janetzke, R. E. Schwirian, A computer program for composing compressor blading from simulated circular-arc elements on conical surfaces, Tech. rep., NASA (1969).
- [45] J. Dunham, CFD validation for propulsion system components (la validation CFD des organes des propulseurs), Tech. rep., Advisory Group for Aerospace Research and Development (AGARD), Neuilly-sur-Seine (France) (1998).

- [46] Langley Research Center, Design study of advanced model support systems for the national transonic facility, Tech. rep., NASA (1987).  
URL <https://books.google.ca/books?id=JL6WuAEACAAJ>
- [47] A. M. Hall, C. Slunder, The metallurgy, behavior, and application of the 18-percent nickel maraging steels, Tech. rep., Battelle Memorial Inst Columbus OH Columbus Labs (1968).
- [48] S. J. Rosenberg, Nickel and its alloys, Tech. rep., National Bureau of Standards Gaithersburg MD (1968).
- [49] J. Campbell, F. J. Barone, D. Moon, The mechanical properties of the 18 per cent nickel maraging steels, Tech. rep., Battelle Memorial Inst Columbus OH Defense Metals Information Center (1964).
- [50] A. Ribes, C. Caremoli, Salome platform component model for numerical simulation, in: Computer Software and Applications Conference, 2007. COMPSAC 2007. 31st Annual International, Vol. 2, IEEE, 2007, pp. 553–564, salome can be downloaded from [www.salome-platform.org](http://www.salome-platform.org).
- [51] A. Sternchüss, E. Balmès, On the reduction of quasi-cyclic disks with variable rotation speeds, in: Proceedings of the International Conference on Advanced Acoustics and Vibration Engineering (ISMA), 2006, pp. 3925–3939, oai: [hal-00266394](https://hal.archives-ouvertes.fr/hal-00266394).
- [52] M. Legrand, A. Batailly, C. Pierre, Numerical investigation of abradable coating removal through plastic constitutive law in aircraft engine, *Journal of Computational and Nonlinear Dynamics* 7 (2011) 011010–1–11, doi: [10.1115/1.4004951](https://doi.org/10.1115/1.4004951) - oai: [hal-00627526](https://hal.archives-ouvertes.fr/hal-00627526).
- [53] M. Legrand, A. Batailly, B. Magnain, P. Cartraud, C. Pierre, Full three-dimensional investigation of structural contact interactions in turbomachines, *Journal of Sound and Vibration* 331 (11) (2012) 2578–2601, doi: [10.1016/j.jsv.2012.01.017](https://doi.org/10.1016/j.jsv.2012.01.017) - oai: [hal-00660863](https://hal.archives-ouvertes.fr/hal-00660863).
- [54] J. D. Denton, L. Xu, The effects of lean and sweep on transonic fan performance, in: ASME Turbo Expo 2002: Power for Land, Sea, and Air, Amsterdam, The Netherlands, 2002, pp. 23–32, GT2002-30327.
- [55] E. Erler, H. D. Vo, H. Yu, Desensitization of axial compressor performance and stability to tip clearance size, *Journal of Turbomachinery* 138 (3) (2015) 031006, doi: [10.1115/1.4031865](https://doi.org/10.1115/1.4031865). doi: [10.1115/1.4031865](https://doi.org/10.1115/1.4031865).
- [56] J. Lainé, E. Piollet, F. Nyssen, A. Batailly, Blackbox optimization for aircraft engine blades with contact interfaces, *Journal of Engineering for Gas Turbines and Power* 141 (6) (2019) 061016, doi: [10.1115/1.4042808](https://doi.org/10.1115/1.4042808) - oai: [hal-02059582](https://hal.archives-ouvertes.fr/hal-02059582).
- [57] E. Erler, Axial compressor blade design for desensitization of aerodynamic performance and stability to tip clearance, Ph.D. thesis, École Polytechnique de Montréal (2012).
- [58] R. Biollo, E. Benini, Shock/boundary-layer/tip-clearance interaction in a transonic rotor blade, *Journal of Propulsion and Power* 25 (3) (2009) 668–677, doi: [10.2514/1.39541](https://doi.org/10.2514/1.39541).
- [59] A. Batailly, A. Millecamps, Minimizing clearance consumption: a key factor for the design of blade robust to rotor/stator interactions ?, in: Proceedings of the ASME Turbo Expo 2016 conference, GT2016-56721, Seoul, South Korea, 2016, p. V07AT32A011, GT2016-56721.